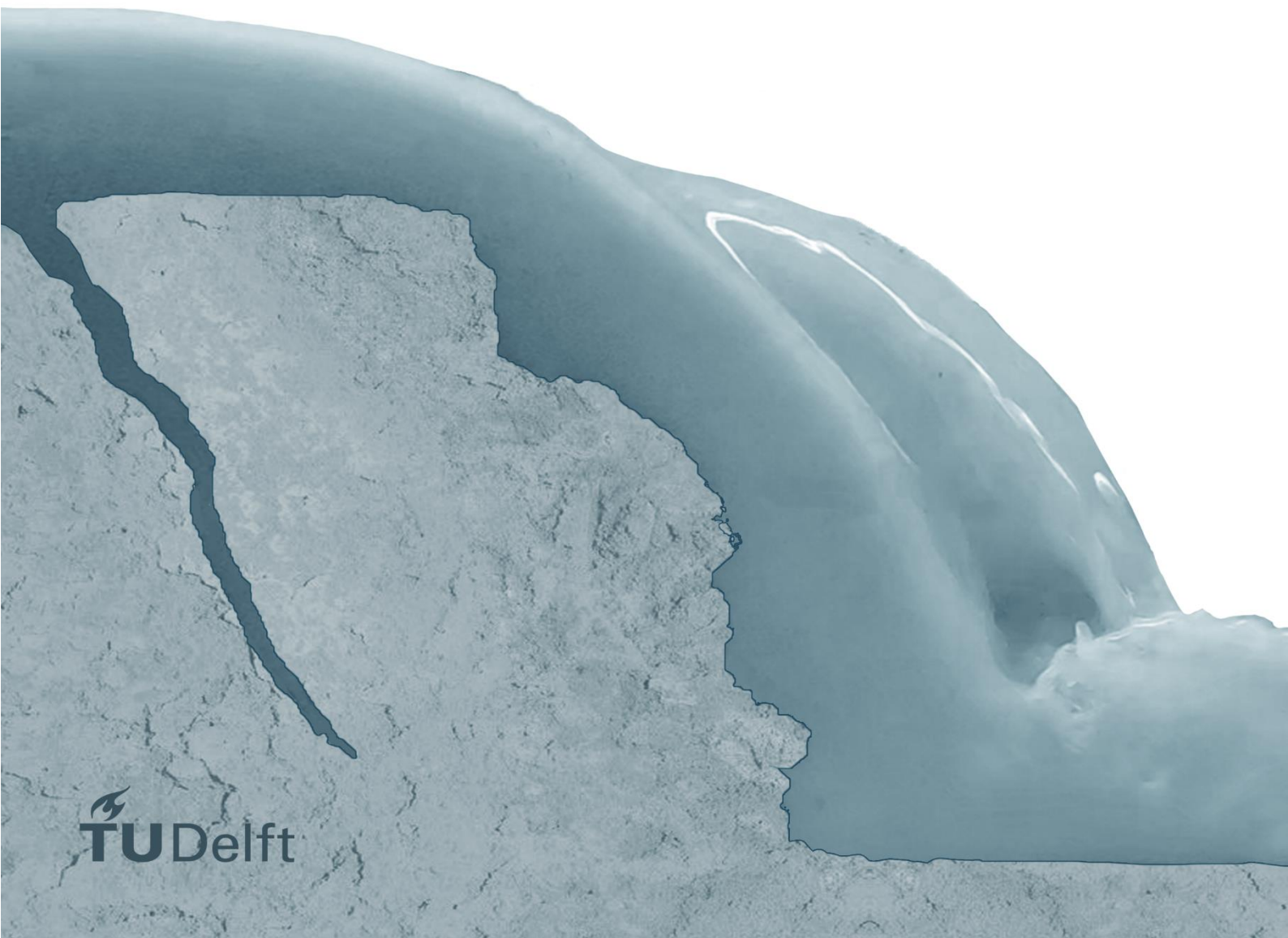


MSc thesis

The stability of foreland types under dike breach conditions – an experimental study

J.S.J. van der Hagen



The stability of foreland types under dike breach conditions – an experimental study

by

J.S.J. van der Hagen

In partial fulfillment of the requirements for the degree of

Master of Science
in Civil Engineering

At the Delft University of Technology,
to be defended publicly on January 20, 2023 at 13:00

Student number: 4355245

Project duration: 15 February 2022 – January 2023

Thesis committee:	Prof. dr. ir. S.G.J. Aarninkhof	TU Delft, Chairman
	Ir. M. van den Berg	TU Delft, Daily supervisor
	Prof. dr. P.M.J. Herman	TU Delft & Deltares, Supervisor
	Dr. ir. S.J.H. Rikkert	Deltares, Supervisor

An electronic version of this thesis is available at <http://repository.tudelft.nl/>.



Preface

This report concludes my Master's degree in Hydraulic Engineering at the Faculty of Civil Engineering at TU Delft. Experiments and tests were conducted for this research in the Hydraulic Laboratory and the Soil Mechanics Laboratory located in the TU Delft Faculty of Civil Engineering and Geosciences.

During these experiments, I worked with many people whom I am grateful for their knowledge, efforts, and time. But also, for the great pleasure we had with the experiments, thinking about the setup, preparing the sediment, and performing the tests.

I would specifically like to thank several people: Ir. Mario van den Berg for the daily supervision; the technical assistants in the Hydraulic Laboratory, Chantal Willems, Pieter van der Gaag, Arie van Vliet, and Arno Doorn for thinking along and helping with building the experimental setup; Christina Cavero Panez from the Soil Mechanical Laboratory for assisting with the clay analyze tests; the supervisory committee Prof. dr. ir. Stefan Aarninkhof (TU Delft), Prof. dr. Peter Herman (TU Delft and Deltares), and Dr. ir. Stephan Rikkert (Deltares). The student assistants (especially Youri Metsch) and friends, literally stood with their feet in the clay for the heavy shovel work and making beautiful images (Iris Jansen). And all other friends and family for the support, stimulation, and relaxation.

I learned a lot from this research, both technically and personally. I would like to conclude with a saying that applies both to this field where urgency is a necessity, but which also applies to me personally: 'Foresight is the essence'.

*Joep van der Hagen
Delft, January 2023*

Summary

Due to accelerating climate change, which entails more extreme storm conditions and exponential sea level rise, the protective function of our dikes and levees is under growing pressure. The presence of so-called forelands (e.g., beach, mudflat, and tidal marsh) are promising Nature-based Solutions to reduce the probability of dike failure and to mitigate the consequences after a dike breach. However, the positive effects of forelands depend, for instance, on sediment composition, geometry, and the presence of vegetation. These effects have not been studied in detail and have not been incorporated into reliable physical and validated mathematical models yet.

This report describes an experimental study on the stability of different foreland types. Particularly, the following aspects were considered: investigating whether surface and headcut erosion are indeed the dominant foreland erosion mechanisms, plus providing experimental data for validation purposes for models such as the extended BRES model.

Twelve experiments were performed in the sediment flume facility of the Hydraulic Laboratory of the faculty of Civil Engineering and Geosciences at the Delft University of Technology. A foreland during breaching conditions (i.e. high flow velocities) was simulated by an experimental setup, a so-called broad-crested weir. This weir was developed, constructed, and built within the facility to simulate and study erosion processes of two foreland sediment types, sand and clay. Geotechnical properties were obtained by performing sediment analyses in the Geoscience and Engineering Laboratory. In order to try to exclude the influence of cracks, a special adjustment of the facility was made by covering the sediment package with plywood panels; these experiments are referred to as ‘Tompouce’. For collecting data, the facility was fully instrumented with hydraulic sensors (discharge, flow velocities, and water levels) and synchronized cameras. The erosion process was analyzed and quantified from the visual data.

The experiments enabled us to answer the main research question, “*Which erosion mechanisms are important to consider for forelands under dike breach conditions?*”. For non-cohesive sediments, surface erosion should be considered the dominant erosion mechanism. In the case of cohesive sediments, however, headcut block erosion should be considered the dominant erosion mechanism. Here, when cracks are present, the erosion rate increases considerably. Especially the latter effect is a new finding; this mechanism should be included in foreland-dike breach development modeling. More research is needed into the quantitative effect of cracks on the stability of a vegetated foreland when it is subject to (sudden) high-water events.

Contents

PREFACE	3
SUMMARY	6
CONTENTS	8
NOMENCLATURE	10
1 INTRODUCTION	11
1.1 RESEARCH CONTEXT	11
1.1.1 <i>Increased Risk of Flooding</i>	11
1.1.2 <i>Dike Failure</i>	12
1.1.3 <i>Forelands as Nature-based Solutions</i>	13
1.1.4 <i>Foreland Sediment Erosion Mechanisms</i>	15
1.1.5 <i>Mathematical Numerical Model Approach</i>	18
1.2 PROBLEM STATEMENT	19
1.3 RESEARCH QUESTIONS	19
1.4 GENERAL APPROACH OF THE STUDY	20
1.5 THESIS OUTLINE	20
2 EXPERIMENTAL SETUP	21
2.1 OVERALL DESCRIPTION	21
2.1.1 <i>Tompouce Experimental Setup</i>	25
2.2 MEASUREMENT TECHNIQUES AND SENSORS	26
2.2.1 <i>Discharge Sensor</i>	26
2.2.2 <i>Electromagnetic Flow Sensor (EMS)</i>	27
2.2.3 <i>Water Level Sensors</i>	28
2.2.4 <i>GoPro Setup and Settings</i>	30
2.3 EXPERIMENTAL PROCEDURE	32
3 EXPERIMENTAL CONDITIONS	35
3.1 SEDIMENT ANALYSIS	35
3.1.1 <i>North Sea sand</i>	35
3.1.2 <i>River clay</i>	37
3.2 EXPERIMENTAL CAMPAIGN	38
3.3 SOIL AND HYDRAULIC CONDITIONS FOR EXPERIMENTS NSS3, RC3 AND TP2	42
3.3.1 <i>Experiment NSS3</i>	42
3.3.2 <i>Experiment RC3</i>	45
3.3.3 <i>Experiment TP2</i>	48
4 EXPERIMENTAL RESULTS AND OBSERVATIONS	51
4.1 RESULTS OF EXPERIMENT NSS3	51
4.2 OBSERVATIONS OF EXPERIMENT NSS3	53
4.3 RESULTS OF EXPERIMENT RC3	54
4.4 OBSERVATIONS OF EXPERIMENT RC3	58
4.5 RESULTS OF EXPERIMENT TP2	60

4.6	OBSERVATIONS OF EXPERIMENT TP2	62
4.7	IMPROVING THE EXTENDED BRES-MODEL	63
5	DISCUSSION	65
5.1	FORELAND STABILITY IN REALITY	65
5.2	THE USE OF A BROAD-CRESTED WEIR AS EXPERIMENTAL SETUP	67
6	CONCLUSIONS	69
7	RECOMMENDATIONS	71
	REFERENCES	73
	APPENDIX A: ADDITIONAL IMAGES	79
	APPENDIX B: INSTRUMENTS	83
	APPENDIX C: AVAILABLE DATA	87

Nomenclature

Dimensionless symbols

Symbol	Description	Unit
C_c	Coefficient of curvature	-
C_d	Discharge coefficient	-
C_u	Uniformity coefficient	-
IC	Consistency index	-
IL	Liquidity index	-
IP	Plasticity index	-
n	Porosity	-

Greek symbols

Symbol	Description	Unit
ρ	Water density	kg/m^3
ρ_{sd}	Dry density	Mg/m^3
ρ_{sw}	In-situ density	Mg/m^3
τ_c	Critical shear stress	kPa
ϕ	Internal friction angle	<i>degrees</i>

Roman symbols

Symbol	Description	Unit
c	Cohesion	kPa
c_u	Undrained shear strength	kPa
D_{90}	Maximum size of the smallest 90% of the sample	mm
D_{60}	Maximum size of the smallest 60% of the sample	mm
D_{50}	Maximum size of the smallest 50% of the sample, median of the PSD curve	mm
D_{30}	Maximum size of the smallest 30% of the sample	mm
D_{10}	Maximum size of the smallest 10% of the sample	mm
F_1 & F_2	Additional horizontal forces	N
g	Gravitational acceleration	$9.81\ m/s$
h_0	Overflow head upstream of the weir	m
h_{1-5}	Water level relative to the flume bottom measured by the five sensors	cm
H	Flume fill water level relative to the flume bottom	cm
K	Coefficient of permeability	mm/s
LL	Liquid limit	%
p	Weir height	$0.55\ m$
PL	Plastic limit	%
Q	Pump discharge	l/s
Q_e	Estimated theoretical flow discharge	l/s
$Q_{e,max}$	Maximum estimated flow discharge during an experiment	l/s
Q_m	Measured flow discharge by the PPF sensor	l/s

$Q_{m,max}$	Maximum measured flow discharge during an experiment	l/s
t	Time	s or $min.$
U	Free flow velocity	m/s
U_c	Crest flow velocity measured on top of the broad-crested weir	m/s
$U_{c,max}$	Maximum measured crest flow velocity during an experiment	m/s
w	Moisture content	%
W	Sediment flume facility width	$0.77\ m$

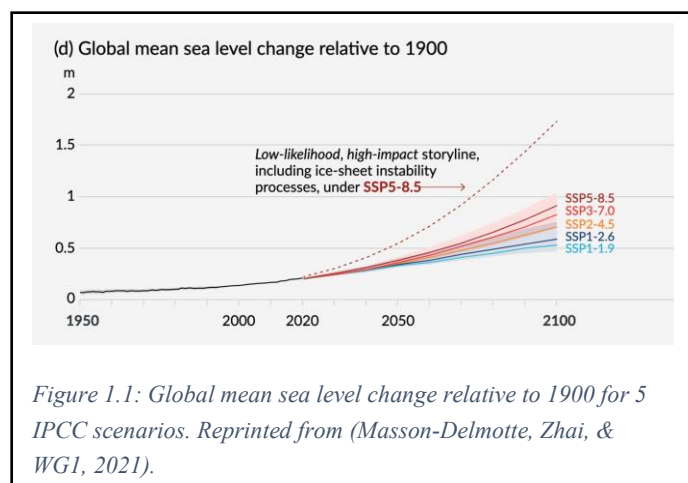
1 Introduction

1.1 Research Context

This chapter presents a literature review of the relevant background information for this study. Based on the review, a problem statement and research questions are formulated. Next, the methodology to answer the research question is given. Lastly, a thesis chapter outline is provided.

1.1.1 Increased Risk of Flooding

Climate change is a continuous process that used to be on timescales of the order of 1,000 to 10,000 years. But since the industrialization of the last century, the increase in greenhouse gas emissions has given a perceptible acceleration to climate change. This now leads to climate change on a much shorter time scale and makes it a lot more difficult for nature and people to adapt properly. The sea level rises exponentially and extreme weather conditions, such as storms, draughts, and excessive rainfall events become stronger and more frequent (Kim & Suh, 2018; Temmerman, et al., 2013). These and other effects of climate change are noticeable on both a continental and regional scale. Many large cities with great economic values are located in deltas, making these areas vulnerable to the increasing risk of flooding (Vrijling, Schweckendiek, & Kanning, 2011). In 2021, the Intergovernmental Panel on Climate Change (IPCC) released a report (Masson-Delmotte, Zhai, & WG1, 2021) containing, amongst others, an updated graphical representation of the historical and the predicted global mean sea level rise with respect to 1900 over the coming decades, see Figure 1.1. From this figure, the scale of the problem we are facing is obvious: a sea level rise of at least 50 cm at the end of this century can be expected.

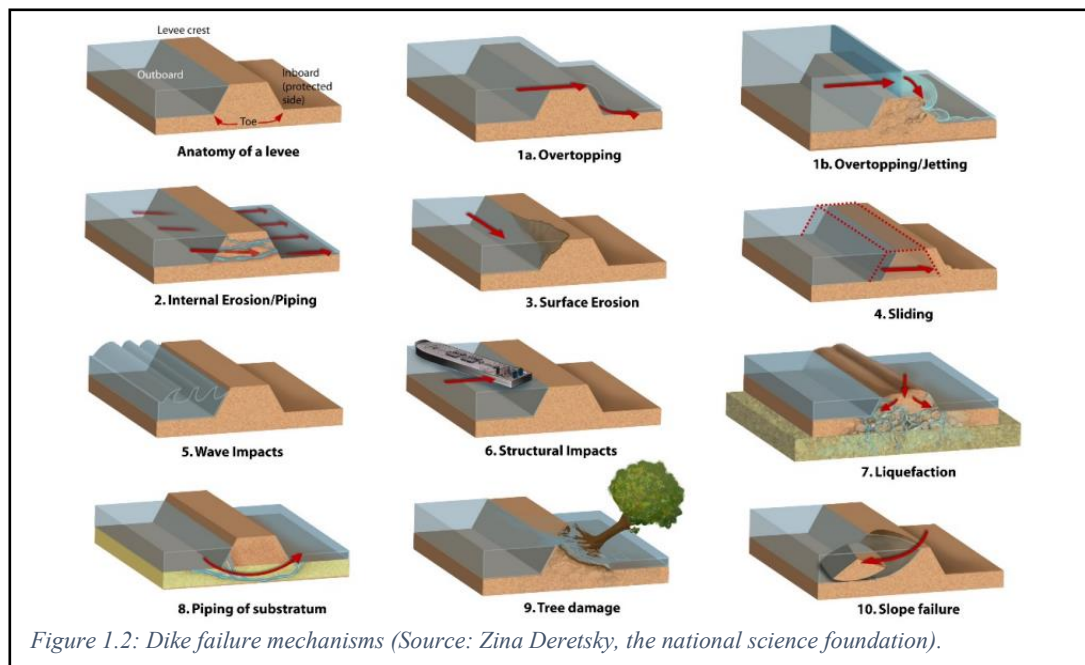


In addition, if the hydraulic conditions are unfavorable in a particularly vulnerable delta, the possible occurrence of sediment scarcity results in a disruption of the sediment source/sink balance and can lead to a major additional problem. The problems demand major efforts in the

field of flood risk management and dike strengthening, to ensure safe living and working in our low-lying polders for present and future generations.

1.1.2 Dike Failure

Conventional flood defenses, such as dikes, have protected deltas against flooding for centuries. However, due to accelerating climate change, the probability of a dike failure and thereby the risk of flooding is a major concern. A dike may fail by various mechanisms (TAW, 1998). The cause is usually related to hydraulic and/or geotechnical failure. Four main failure mechanisms can be distinguished: overtopping, macro-stability, waterside erosion, and piping. Figure 1.2 shows illustrations of these and other known failure mechanisms.



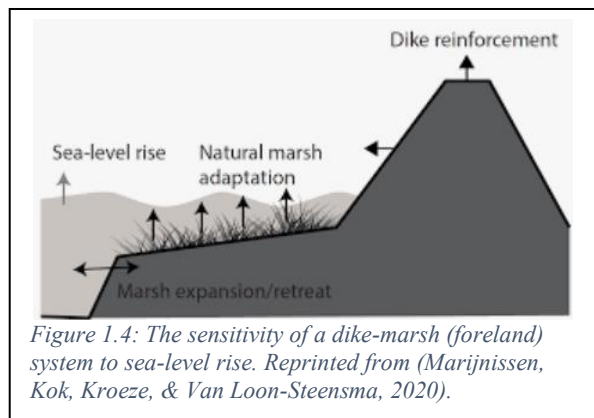
When one or more of these failure mechanisms have caused such damage that the water-retaining function of the dike is lost, a breach starts to develop and inundation of the low-lying hinterland follows (Van Gerven, 2004; Visser P., 1998). Historically, floods resulted in major losses of life and economical damage. In the Netherlands, two well-known floods are the Sint-Elisabeth flood of 1421, which flooded about 28 villages with dozens of drowning victims (Schierreck & Visser, 2021), and the Big Flood disaster of 1953, causing 1836 deaths and a total damage cost of 5.4 billion euro (Gerritsen, 2005).

The common method to strengthen dikes in the past is to heighten and/or widen them. So far, this method was structurally and economically feasible. Recently this method has become a more costly and space-consuming engineering strategy, as both the extreme hydraulic loads, as well as potential consequences are increasing. Moreover, the concept of sustainability was not taken as seriously as it is now. New methods to ensure adequate flood safety is required.

1.1.3 Forelands as Nature-based Solutions

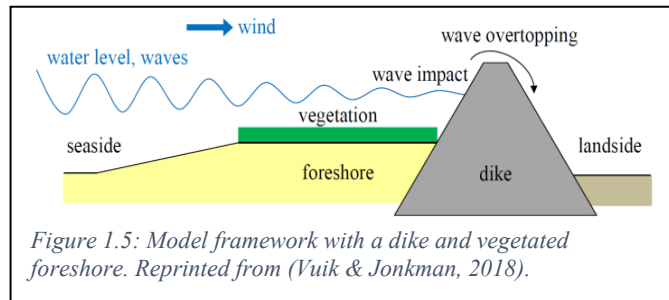
Due to climate change and the impending infeasibility of continuous dike reinforcement, engineers have started to implement important properties such as sustainability and adaptability in the design and development strategy of flood defense systems. Nature-based solutions are a powerful tool that embraces this engineering strategy. These solutions use natural systems to provide a wide range of benefits, including cleaner air and water, improved soil health, and increased biodiversity. They can also help to reduce greenhouse gas emissions and protect against extreme weather (Laboyrie, et al., 2018). While developing a natural flood protection system, important factors are that nature can take its course as much as possible and ecosystems should be protected sufficiently for a considerable time to be able to fully develop. (De Vries, Van Koningsveld, Aarninkhof, & De Vriend, 2021).

A recently rediscovered example of such a Nature-based Solution is creating a so-called foreland. A foreland is an elevated area (e.g., beach, mudflat, and tidal marsh) on the seaward or river side of a dike/levee. Forelands have a self-sustaining property. Self-sustaining in the sense that sedimentation of the foreland follows the rising sea level, see Figure 1.4 (Marijnissen, Kok, Kroeze, & Van Loon-Steensma, 2020). When the morphological conditions are favorable, a foreland may grow through different phases with respect to soil type: starting from a sandy ecosystem (nourishment), via silt, towards a mudflat. Eventually, seeds might germinate and a fully grown salt marsh can be its final, robust stage. Figure 1.3 shows an example of a vegetated foreland in the Netherlands applied in innovative dike reinforcements to increase flood safety.



From previous research, three promising results on the relative benefits of creating forelands as a Nature-based Solution have already been found.

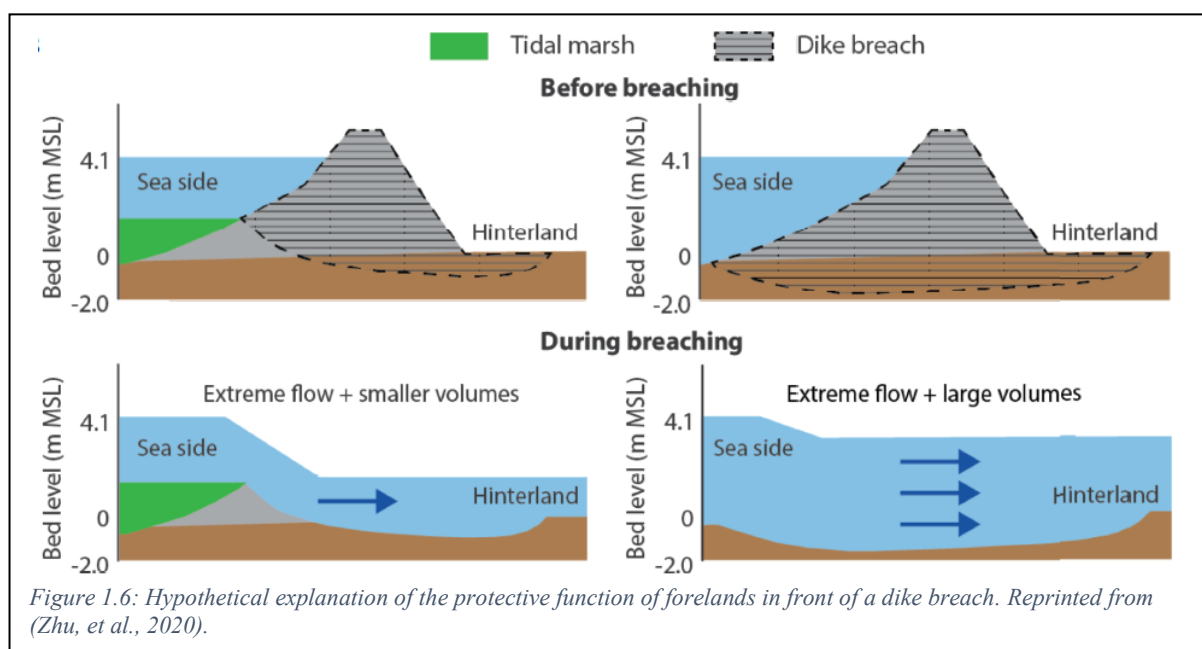
Firstly, waves energy dissipates the shallow water overlying the foreland before they reach the dike, see Figure 1.5. As a result, the wave loads on dikes is dampened and therefore the probability of dike failure is reduced (Vuik, Jonkman, Borsje, & Suzuki, 2016).



Secondly, the volume of water flowing through a breach decreases when a foreland is present, see Figure 1.6. This reduces the erosion rate of a dike and reduces the inundation rate of the hinterland (Zhu, et al., 2020). Consequently, flood risk is reduced since more time is available for intervening in the breach and for evacuation.

Lastly, the flow through the breach and inundation of the hinterland stops when a storm subsides and the water level falls below the foreland surface level. Of course, in a severe case, where the foreland is eroded completely during a storm, this advantage does not exist any longer.

To estimate the reliability of these predicted advantages of forelands, it is necessary to investigate the stability of forelands, i.e., to what extent they resist erosion.



1.1.4 Foreland Sediment Erosion Mechanisms

The stability of a foreland can be translated into the presence and influence of erosion mechanisms. Until now, two main types of foreland erosion mechanisms are known to be relevant and have been included in mathematical-numerical modelling: surface erosion and headcut erosion. For foreland surface erosion, a distinction is made between non-cohesive (sand) and cohesive (clay) sediment.

Surface Erosion; non-cohesive material

When water flows over a foreland sediment bed which contains coarse material (non-cohesive), the water gradually penetrates the bed. If the bed shear stress becomes larger than its critical value, the sediment bed erodes layer by layer. This process results in degradation of the bed to a critical angle. The eroded sediment is washed away as suspended load through the breach and deposits in the hinterland where the flow decelerates.

In literature, many sediment transport formulas can be found as an application to sand-dike breach erosion to calculate the sediment transport capacity. Each formula has been developed and calibrated for specific data sets/regimes, see (Visser, 1995). The formulas have in common that they all work with a certain grain diameter and use the well-known formulations of Shields (Shields, 1936) and Isbash (Isbash, 1932) as underlying basis. Within this study, four sediment transport formulations are relevant: the formulas of (Engelund & Hansen, 1967), (Van Rijn, 1984), Bagnold-Visser (Visser, 1988), which uses the energetic approach, and (Wilson & Nnandi, 1992). For more detailed information see the original publications referred to.

During a dike breach, the foreland surface is exposed to extreme hydraulic conditions in which flow velocities of for instance 7 m/s can be reached for a 10 m high dike. This super-critical flow regime influences the behavior of the surface erosion mechanism and makes accurate prediction of sediment fluxes difficult. For non-cohesive material, the phenomenon of dilatancy could play a role in retarding the surface erosion rate. Dilatancy refers to an increase in pore volume during shear deformation. A negative pore pressure develops which stabilizes the soil, see also (Alhaddad, 2021; Bisschop, Miedema, Visser, Keetels, & Van Rhee, 2016).

Surface Erosion; cohesive material

When a foreland consists of cohesive (muddy) sediment, water cannot penetrate the sediment bed and a different surface erosion process takes place. Chunks of sediment are eroded due to irregularities and instabilities in the sediment bed, which is called mass (bulk) erosion. We define mass erosion as an undrained erosion process, thus at large Péclet numbers. The Péclet number is a dimensionless number and is defined as the ratio of the advective transport rate by

the diffusive transport rate. The advective transport rate dominates in these high flow velocity regimes.

To determine the mass erosion rate, the expression of Partheniades is used as the basic formulation, see also (Partheniades, 1962). To quantify a possible presence of mass erosion, (Winterwerp, Van Kessel, Van Maren, & Van Prooijen, 2021) formulated a mass-erosion criterion with respect to the hydraulic conditions and bed soil property.

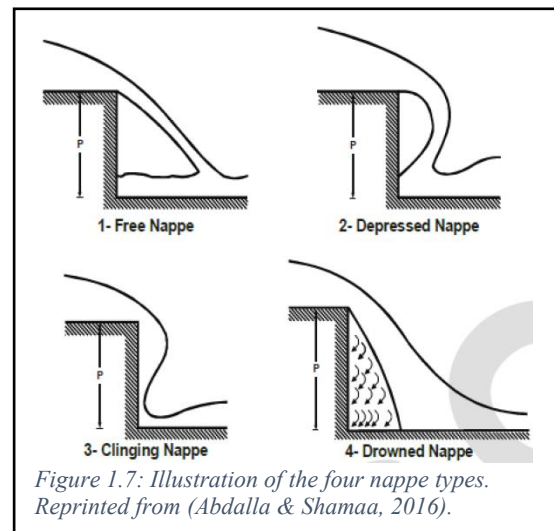
$$\frac{1}{2}\rho U^2 > 5c_u \quad (1.1)$$

With free flow velocity, U (m/s), water density, ρ (kg/m³), and undrained shear strength, c_u (kPa), a geotechnical property of the soil.

Biology (worms, clams, etc.) existing on forelands can play a role in making the bed more inhomogeneous and increase the sediment permeability by making burrows in the system (Volkenborn, Polerecky, Hedtkamp, Van Beusekom, & De Beer, 2007). The disadvantageous consequence of this is that penetration of the fast-flowing water into the foreland surface takes place more easily during a breach. This increases the mass erosion rate and destabilizes the foreland.

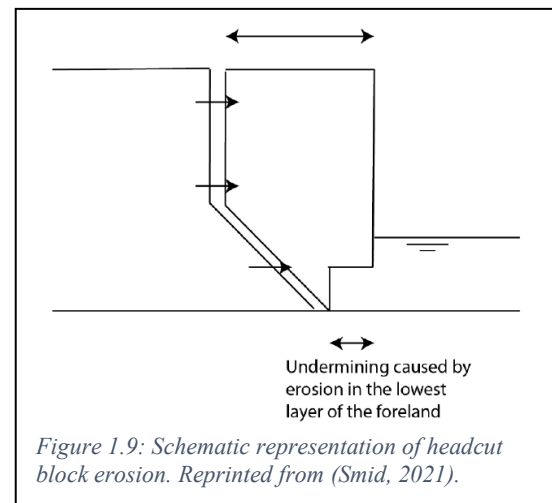
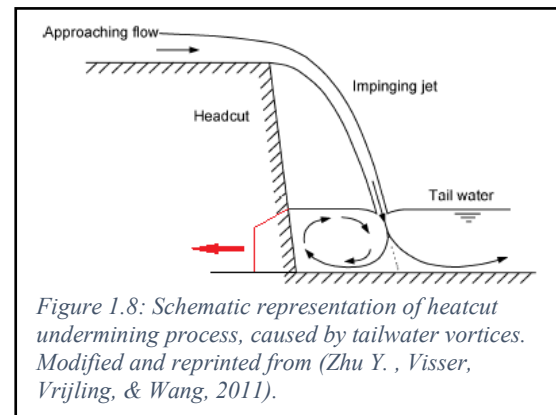
Headcut Erosion

The slope of a foreland consisting of cohesive material does not erode to a critical angle but forms a sudden considerable bed level change, the headcut. When the fast-flowing water reaches the headcut brink it separates from the bed. The water flow forms an overflow jet (free fall), a so-called nappe, which impinges the tailwater downstream of the headcut. A nappe is the phenomenon of an aerated or non-aerated overflow jet. Based on the cavity condition under the nappe, (Abdalla & Shamaa, 2016) classify four types of nappe, see Figure 1.7.



The nappe jet is diverted when it impinges on the tailwater downstream of the headcut. Eddies occur in the tailwater column under the nappe. Due to these vortices the headcut tailwater section erodes, see Figure 1.8. The headcut erosion mechanism depends on the erodibility of the headcut foundation; in this study a non-erodible foundation is considered. For the erodible foundation case, see the analysis of jet scour by (Stein, Julien, & Alonso, 1993).

When the undermining has migrated to a certain distance, a block with a certain width becomes unstable and fails because the acting forces (weight and hydraulic forces) become larger than the resistive forces (soil interaction forces) (Zhu, Visser, & Vrijling, 2006; Robinson & Hansen, 1994), see Figure 1.9. When the block is completely torn off it falls into the tailwater section and is washed away. This periodic event is being amplified in the presence of cracks in the top layer. Cracks and their formation turned out to be essential for this study.



A remaining question is whether surface erosion and headcut erosion are the dominant mechanisms influencing foreland stability.

1.1.5 Mathematical Numerical Model Approach

BRES model

Many mathematical and/or numerical models have been developed to predict breach growth. A well-known, often applied model, is the BRES model (BReach Erosion in Sand-dikes model), developed by (Visser, 1998). In this 1-D mathematical model the breach growth process of a sand dike is described in 5 separate phases, see Figure 1.10. In terms of sediment transport formulas, the model uses Bagnold-Visser (Visser, 1988) for the first three phases (supercritical flow), and Van Rijn (Van Rijn, 1984) for the subsequent phases. The sediment transport is only computed for non-cohesive material. The model distinguishes three types of breaches, which describe a different situation: (A) with the presence of a toe construction in front of the dike, a choice can be made between an erodible or non-erodible foundation, (B) with a relatively high foreland or (C) without any added construction.

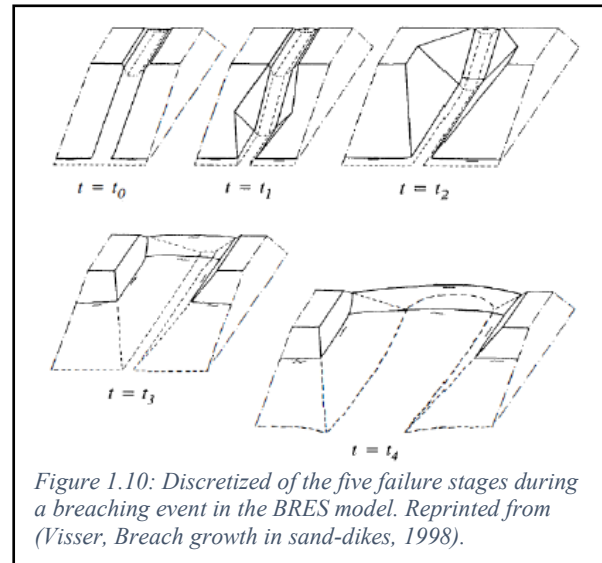


Figure 1.10: Discretized of the five failure stages during a breaching event in the BRES model. Reprinted from (Visser, Breach growth in sand-dikes, 1998).

BRES-2021 module

Recently, the influence of a foreland was added as a separate module in the BRES model by (Smid, 2021). The module is activated from the moment onwards where foreland erosion occurs, which is from phase three in the original BRES model type B. With a mathematical script of the headcut erosion mechanism as described above, the amount of headcut erosion for different scenarios is calculated. Simultaneously, the shape of the foreland spillway is predicted. Four scenarios can be created by the user by selecting between either a sliding or rotating block failure mechanism during the headcut erosion process. A foundation that is or is not erodible is optional when choosing a block failure type, see Figure 1.11.

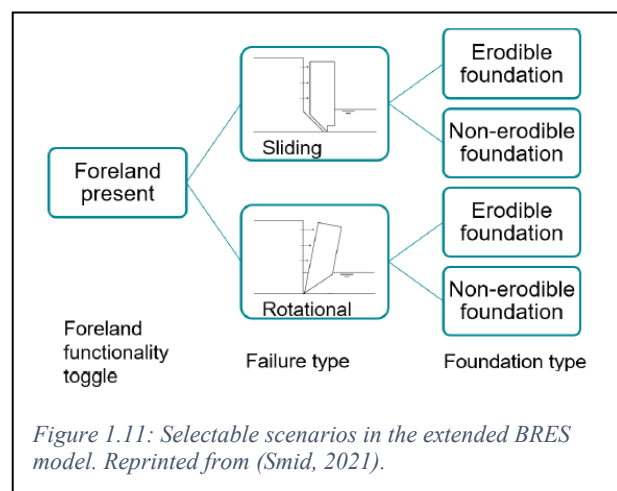


Figure 1.11: Selectable scenarios in the extended BRES model. Reprinted from (Smid, 2021).

The BRES-2021 module takes a simplified approach by means of a uniform soil layer, a single particle size, with no other elements (stones, roots and/or micro-organisms). This does not reflect reality: different sediment types and inhomogeneities will make a difference in foreland stability.

To study the effect of inhomogeneities of the sediment on foreland stability and to validate the BRES-2021 module, data from physical experiments are needed.

1.2 Problem Statement

As we have seen, forelands are promising Nature-based Solutions to reduce the probability of dike failure and to mitigate the consequences after a dike breach. This role largely relies on the stability of the foreland before and during breaching conditions. The latter effect, however, has not been incorporated into reliable physical and numerical models yet and further research in the future will fill this missing knowledge. Moreover, the positive effects of forelands depend on the sediment composition, geometry, and the presence of vegetation, amongst others.

Consequently, our problem statement is twofold:

- (1) Verification is needed whether surface erosion and headcut erosion are indeed the two dominant mechanisms for foreland stability.
- (2) As to modelling, data from physical experiments is needed to study the effect of inhomogeneous sediment and to validate the extended BRES-model.

1.3 Research Questions

To address these problems, the following main research question is formulated:

Which erosion mechanisms are important to consider for forelands under dike breach conditions?

To answer this question, the following sub-questions are formulated:

1. Which erosion mechanisms can be observed under dike breach conditions?
2. Which of these mechanisms is most dominant for sand and which one for clay during breach conditions?
3. Which foreland sediment type: sandy, muddy or vegetated is most suitable to reduce flood risk?

1.4 General approach of the study

The answers to these questions were obtained by developing and instrumenting an experimental setup and by conducting experiments on two sediment types, reflecting two typical stages in the development of a foreland. The resulting experimental data serve three purposes:

- answering the research questions;
- generating insight for building physical models;
- providing data for validating the extended BRES model.

Experiments were performed in the sediment flume facility of the Hydraulic Laboratory of the faculty of Civil Engineering and Geosciences at Delft University of Technology. A foreland during breaching conditions (i.e. high flow velocities) is simulated by an experimental setup, a so-called broad-crested weir. This weir is developed, constructed, and built within the facility to simulate and study erosion processes of two foreland types, sand and clay.

For collecting data, the facility is fully instrumented with hydraulic sensors (discharge, flow velocities and water levels) and synchronized cameras. The erosion process is analyzed and quantified from the visual data.

1.5 Thesis Outline

This thesis is structured as follows:

A description of the experimental setup is given in Chapter 2. The experimental conditions for the twelve experiments performed can be found in Chapter 3. Chapter 4 presents the experimental results obtained; relevant observations and a proposal for an improvement of the extended BRES-model are mentioned as well. The overall findings and limitations when performing foreland stability experiments in the sediment flume facility are discussed in Chapter 5. Conclusions are drawn and summarized in Chapter 6; also, the research questions are answered in this chapter. Finally, suggestions for further research are given in Chapter 7.

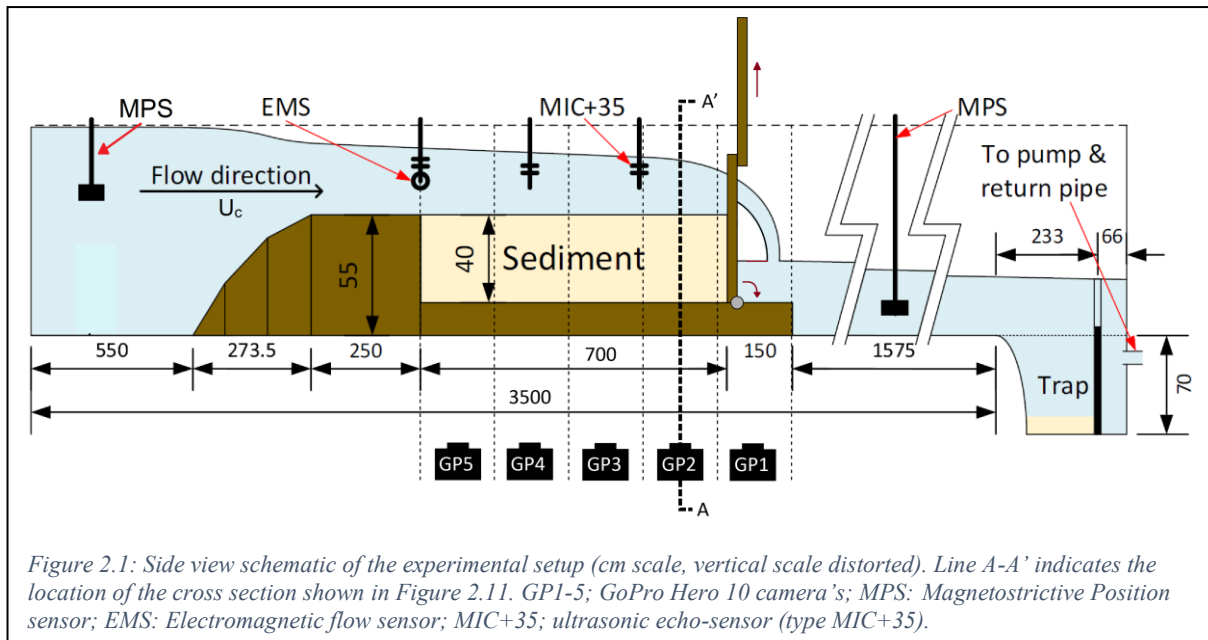
2 Experimental Setup

This chapter gives an extensive description of the experimental setup. Firstly, the sediment flume facility and the developed elements are described and explained. An extensive overview sketch is also shown for clarification. The additional adjustments made for the Tompouce experiments are mentioned separately. Secondly, the measuring techniques used and instruments along with their characteristics, are explained. Finally, a flow chart is provided containing the necessary consecutive steps for a successful experiment and for collecting usable data.

2.1 Overall Description

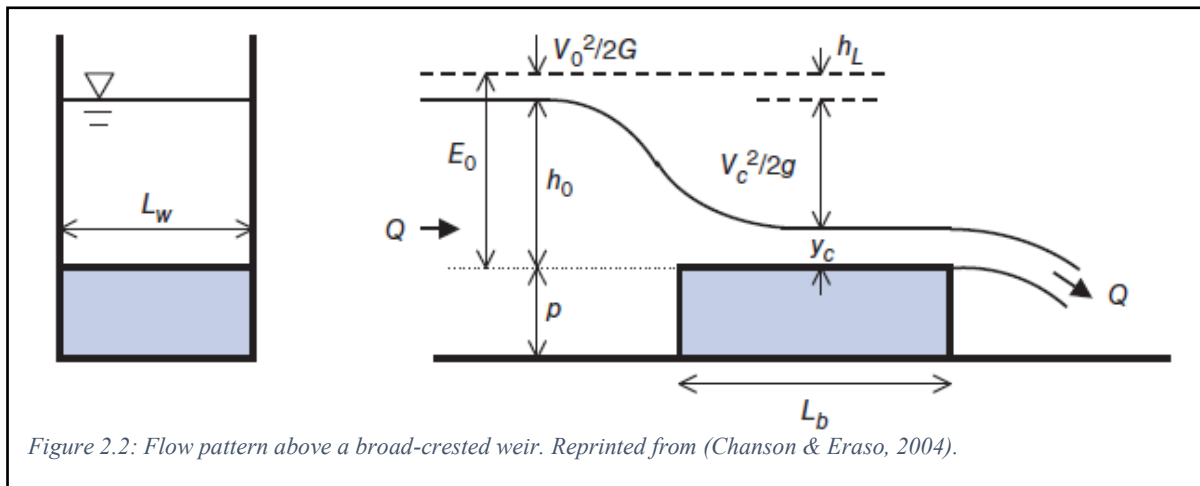
For this study, the sediment flume facility was used to perform experiments. The facility encompassed enough work space and ease of use to properly perform the experiments and carefully prepare the sediment package. The facility itself has dimensions of $0.77\text{ m} \times 0.84\text{ m} \times 40\text{ m}$ (width \times height \times length) and consists of a concrete floor bottom and two sidewalls made of plexiglass panels. These panels are glued together and held by metal frames. Seen from the outside, these metal frames form windows of $143.5\text{ cm} \times 76.5\text{ cm}$ (width \times height). Through these windows, sediment erosion processes can be properly observed from a 2-D perspective by means of cameras. Five windows were used for visual observations with GoPro cameras. With GoPro 1 (GP1) positioned in front of window 1, GoPro 2 (GP2) in front of window 2, and so on.

Figure 2.1 shows a schematization of the full sediment flume facility length of the experimental setup used in this study. The schematic clearly shows the overall experimental setup, measuring instruments, GoPros and the flume system which regulates the hydraulic conditions. Horizontal distances are in centimeter scale and have been added to the schematization. The vertical scale is distorted. A line is drawn to indicate cross-section A-A' at the GoPro 2 position, which will be discussed in Section 2.2.4. Additional images of the experimental setup can be found in Appendix A: Additional Images.



For the experimental setup, specific elements were applied, developed and built within and around the sediment flume facility. The elements were developed to establish foreland-dike breach conditions (high flow velocities) and to observe the sediment stability from a 2D perspective. Concrete plywood panels were used to manufacture all experimental elements. Concrete plywood is a sheet material that consists of several layers of veneer. The sheet material is provided with an epoxy layer. This hard layer forms a waterproof finish which makes it extremely suitable for constructions in humid environments. It is also very easy to treat. Below a short description is provided of the specific elements:

- A broad-crested weir (BCW) with specific characteristics (sketched in brown in Figure 2.1) was developed, constructed, and built within the sediment flume facility to imitate a foreland and the associated hydraulic conditions. Weirs have been extensively used in experimental facilities to study flow conditions in open channels (Badr & Mowla, 2014) (Osman Akan & Iyer, 2021). The essence of a broad-crested weir is that the streamlines on the crest become horizontal and parallel due to the conservation of energy (Chanson & Eraso, 2004). This flow condition also prevails on a foreland during a dike breach. Figure 2.2 shows the typical flow/energy profile over a broad-crested weir. As can be seen, the water level upstream of the weir is raised, which gives an increase in the potential energy. As a result, the discharge on the crest of the weir is maximized. If the crest is long enough (L_b in Figure 2.2), eventually a critical flow will develop on top of the weir. At the downstream end of the weir the water flow detaches from the headcut brink, resulting in an overflow jet. Sufficient space is required upstream and downstream of the weir to allow flow conditions to be set and to minimize the impact of disturbances.



A weir is classified as broad-crested if the crest length is 3 times larger than the critical crest flow depth. To comply with this for the experiments, the developed weir had to have a total length of 1373 cm. To minimize energy loss, the construction had a slope upstream ensuring a gradual bed level change. The slope continued horizontally up to a height of 55 cm, with a total length of 523.5 cm. A false bottom with a height of 15 cm and a total length of 3650 cm was connected to this first part. On this false bottom, the falling gate construction was mounted, and the sediment package could be prepared. This sediment package, together with the upstream slope, gave the necessary extension of the crest to realize the mentioned critical flow condition. The entire BCW construction was hollow. All the concrete plywood panels were glued to each other and to the plexiglass flume side walls. Spaces were retained to allow air to escape during the sediment flume water filling procedure, preventing damage from possible overpressure.

- The sediment package (sketched in beige in Figure 2.1), had a total height of 40 cm, a length of 700 cm, and covered the full sediment flume width. The package was positioned on top of the BCW false bottom, between the ramp and the falling gate, which provides an extension of the BCW crest. At 700 cm, the package covered just over five windows of the sediment flume facility. Care was taken as much as possible to level the surface of the sediment package with the height of the BCW ramp upstream (40 cm), resulting in a horizontal slope up to the headcut. An accelerating crest flow velocity was thereby prevented. The transition of material types between the ramp and sediment surface caused a difference in shear stress in the flow direction, which had consequences during experiments.
- A rotating falling gate structure (sketched in brown in Figure 2.1) was developed and constructed to the right of the sediment package. The falling gate was mounted via a hinge to the false bottom and is held up by a vertically moving lock. This combined construction

created a water level difference. A square passage was made in the lock to let the water flow through. Fine meshes were attached to the side edges to prevent the escape of sediment. A lead block was attached to the downstream side of the falling gate for extra downward fall force during an experiment. The falling gate ensured that the sediment headcut had an initial vertical slope. An experiment starts by lifting the lock.

- Concrete plywood panels were glued on top of the sediment flume sidewalls from the upstream inlet to the end of the BCW false bottom (not shown in the figure). These panels ensured that the water level upstream could be raised even more, which gave extra potential energy, without flooding the facility. The hydraulic measuring instruments and the GoPro setup construction were mounted on top of the panels.
- The sediment was trapped at the far downstream end position of the sediment flume. The water was circulated by a frequency controlled, hydraulic pump (right in Figure 2.1). A piping system fed the water back to the inlet, thereby creating a closed circulating system. A disadvantage of such a closed system is that fine material is circulated, making the water more and more turbid during consecutive experiments.
- Drifting block elements were installed at the most upstream and downstream position of the sediment flume (not shown in the figure). These blocks dampen the waves formed by the waterflow inlet and BCW.

2.1.1 Tompouce Experimental Setup

After three river clay experiments, an adjustment of the facility has been made. The adjustment ensured, among other things, that mass surface erosion was excluded, which had a major impact on the headcut erosion process. And it allowed an aerated nappe to develop properly. As a result, headcut erosion, caused by undermining alone and as calculated in the BRES-2021 module, could be carefully analyzed.

A single layer of concrete plywood panels was constructed on top of the clay package (see Figure 2.3). The panels served as an extension of the BCW concrete plywood ramp surface height all the way until the clay package headcut (see Figure 2.4). To prevent the panels from floating during experiments, they were attached to the sediment flume side walls by means of small flow-conducting panels (see Figure 2.4 and Figure 2.5). The false bottom, yellow plus-grid and two measurement devices can also be observed in the images. The name “Tompouce” is chosen because the layered structure resembles a typical Dutch pastry named Tompouce (or Tompoes), consisting of puff pastry on top of cream. Below three images are shown to give an impression of the Tompouce experimental setup.



Figure 2.3: Image of placing the concrete plywood panels on top of the river clay package.



Figure 2.4: Side view image of the Tompouce experimental setup taken at the headcut location. The false bottom and yellow plus-grid can be observed as well.

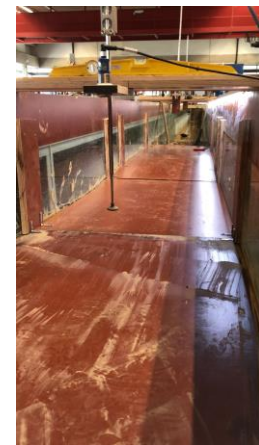


Figure 2.5: Top view image of the Tompouce experimental setup taken within the sediment flume facility. A water level sensor (MIC+35) and flow velocity sensor (EMS) can be observed as well.

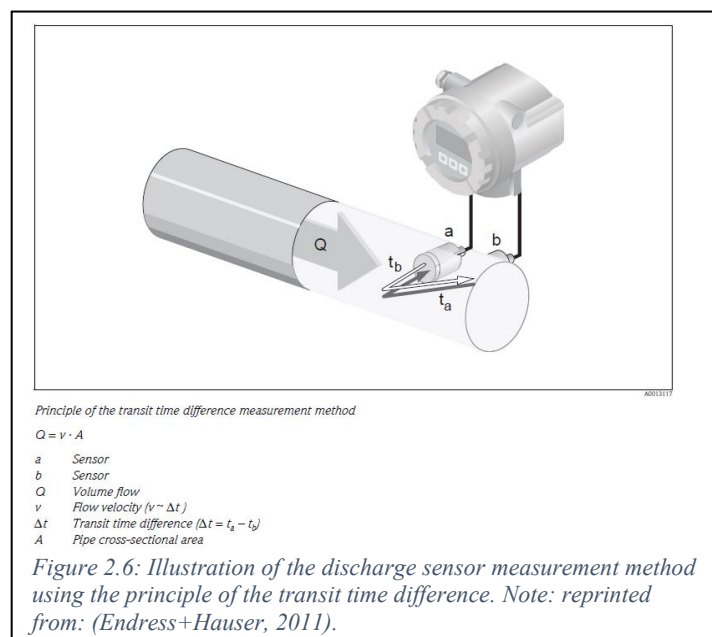
2.2 Measurement Techniques and Sensors

A range of measuring devices was used during the experiments, including a discharge sensor, a flow velocity sensor, water level sensors and GoPros for visual inspection. All measuring devices are owned by the Hydraulic Laboratory. First, the installation and specifications of each hydraulic measuring sensor is described separately. Images of the installation and position of the sensors in the sediment flume facility can be found in Appendix A: Additional Images. Thereafter, the GoPro setup is described, and its installed settings are mentioned.

By measuring the water level at specific locations, upstream, downstream and at the top of the BCW, the water surface profile/progression of the energy head (Figure 2.2) and gradient are known along the entire sediment flume length. Together with the measured flow rate and the flume width, the local flow conditions can be determined. The local flow conditions in the context of the headcut, together with the theory, provide input for the extended BRES-model. The data of the hydraulic measuring sensors are recorded and stored using the program DASYlab on a computer in the Hydraulic Laboratory for further analyses. In this program, the measuring frequency was set to 10 Hz for all instruments. The signals of the hydraulic measuring devices are voltage outputs. These outputs were converted into the correct unit through calibrations. The obtained calibration factors were implemented in DASYlab. Specifications and graphs made for the calibration per instrument type are shown in Appendix B: Instruments.

2.2.1 Discharge Sensor

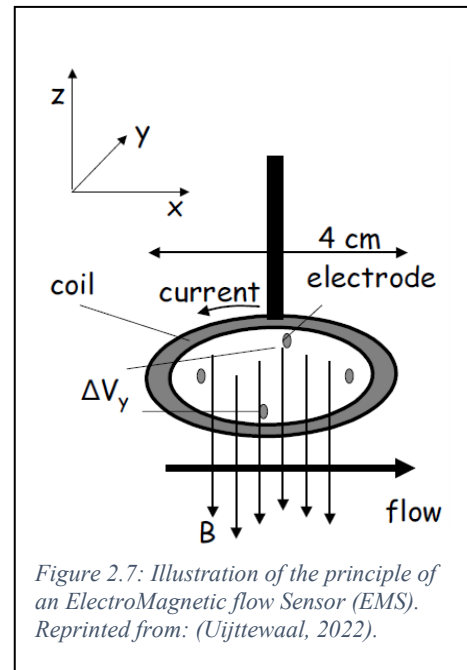
The discharge was set by adjusting the frequency of the hydraulic pump. The actual discharge was measured by a Proline Prosonic Flow 91W ultrasonic flowmeter (abbreviated as PPF). The sensor is situated in the return flow pipe under the sediment flume facility. It measures the flow velocity using the principle of transit time difference. The measured flow velocity was converted to a discharge value (see Figure 2.6).



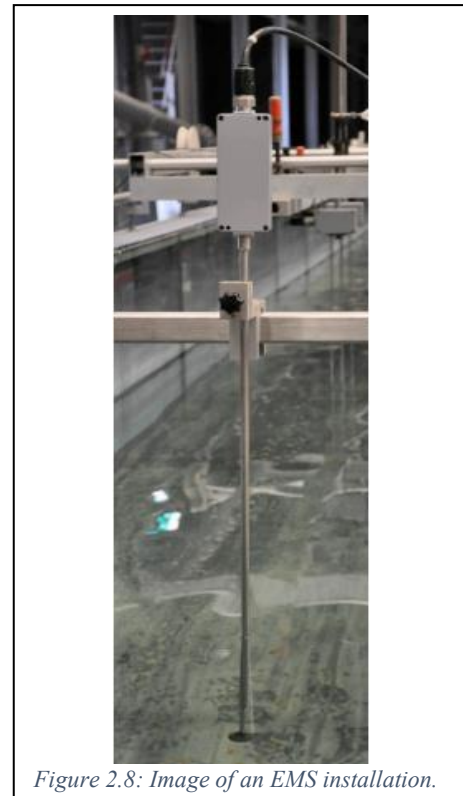
For more technical information see the Endress+Hauser documentation (Endress+Hauser, 2011).

2.2.2 Electromagnetic Flow Sensor (EMS)

To measure the crest flow velocity (U_c), an Electromagnetic flow sensor (abbreviated as EMS) was used. Figure 2.7 provides a sketch of the principle of an EMS (Uijtewaal, 2022). The water flows through a magnetic field (B) which is induced by an electrical current in a small coil inside the body of the probe of the instrument. Due to the charge carried by the water flow a potential difference (ΔV_y) is created which is proportional to the flow velocity. To prevent disruption of the water flow as much as possible, the narrower E30 probe type is used. This probe type is connected to a control unit with a measuring range of 0 – 2.5 m/s. The calibration certificate of the specific EMS model provided by Deltares (see Appendix B: Instruments) was used to convert the analogue output signal (volts) to a velocity, U (m/s) in the program DASYlab.



The EMS was installed at the upstream location of the broad crested weir. It was attached to an adjustable mount to have control over its vertical position. This is necessary because the E30 probe has a minimum immersed depth of 5 cm. Figure 2.8 shows an image of the installation of an EMS. For the position and installation in the sediment flume facility see Appendix A: Additional Images. For more technical information see the Deltares documentation (Deltares, 2022).

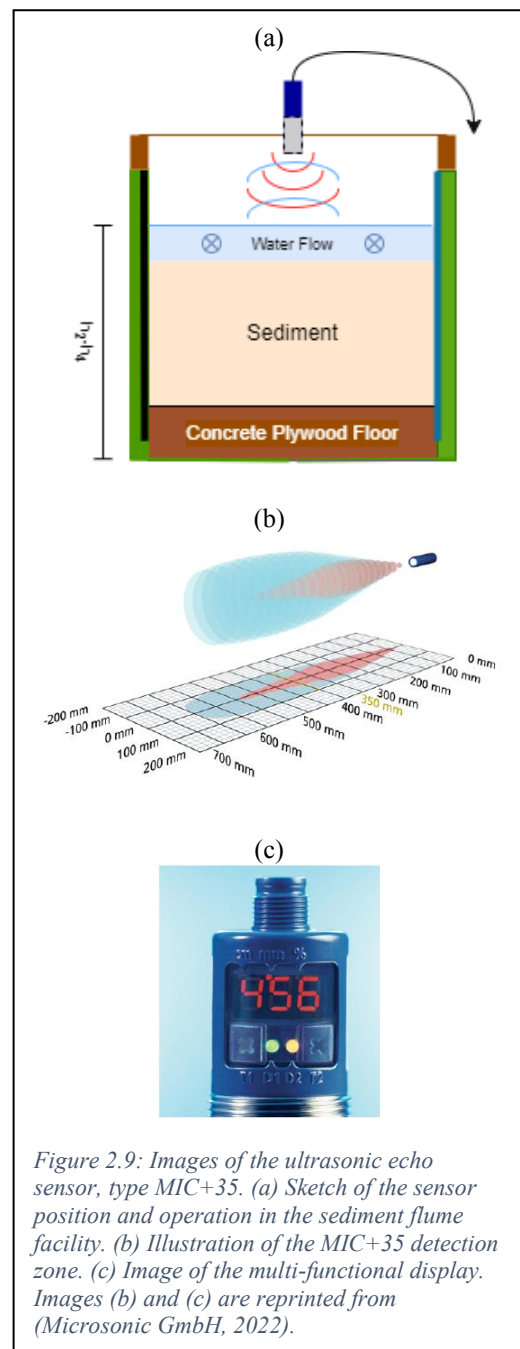


2.2.3 Water Level Sensors

Five position sensors were used to measure the water level relative to the sediment flume bottom (h_1 - h_5). Three ultrasonic echo-sensors (type MIC+35, abbreviated as MIC) and two Magnetostrictive Position Sensors (abbreviated as MPS) are installed in the sediment flume facility. The positioning of the sensors is chosen such that the water level profile over the full sediment flume length is known.

Ultrasonic echo-sensor

The three ultrasonic echo-sensors were evenly installed over the BCW sediment package. The second and third echo-sensors were attached to adjustable mounts, to have control over their vertical position (see Appendix A: Additional Images). The sensors were fixed to the concrete plywood by means of their screw thread. A sensor determined the distance to the water surface via echo propagation time measurements. Because the height of the sensors and sediment package is known, the water level relative to the sediment flume bottom can be obtained (h_2 - h_4). Sensor type MIC+35 was used, which has a detection zone of 65 to 600 mm. The cylindrical sensor has a touch control with a LED display which shows the direct measured value output in mm/cm or %. Via two keys the pre-settings can be changed (see also Figure 2.9 (a, b and c)). Calibrations of the three sensors were performed to convert the analogue output signal (volts) to distances (cm) (see Appendix B: Instruments). For more technical information, see the document of the manufacturer Microsonic (Microsonic GmbH, 2022).



Magnetostrictive position sensor

The two magnetostrictive position sensors were installed at the far upstream and downstream end in the sediment flume facility. These sensors were clamped below their electronics housing as tight as possible to prevent shifting (see Appendix A: Additional Images). The Model GH rod-style sensor was used. They consist of two elements: (1) A waveguide sensor (stroke), which induces a magnetic field. (2) A magnet float (ball, diameter is 53 mm), which passes along the outside of the sensor. The position of this magnet float was determined. Because the height of the sensor and the stroke length is known, the water level relative to the sediment flume bottom can be obtained (h_1 and h_5). A Styrofoam block was attached around the middle of the magnet floating ball for stabilization, which kept the water level measurement results as constant as possible during high flow velocities and in case small waves were generated downstream (see Figure 2.10 (a, b, and c)).

For more technical information see the document of the manufacturer Temposonics (Temposonics GmbH & Co. KG, 2015).

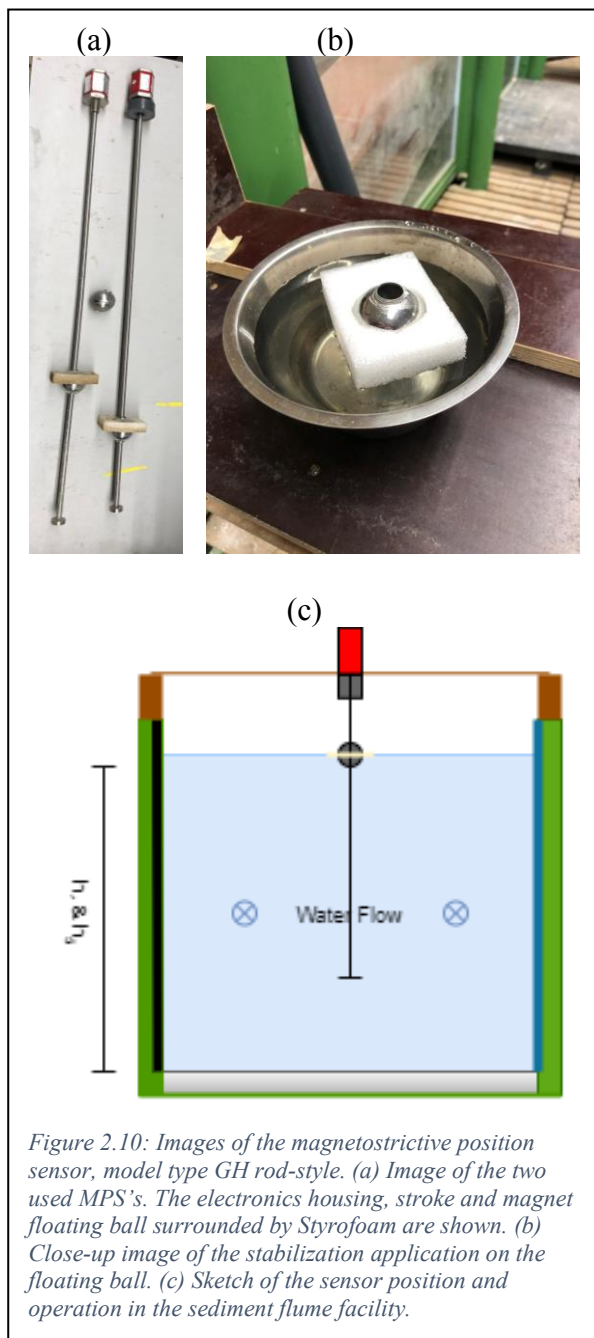
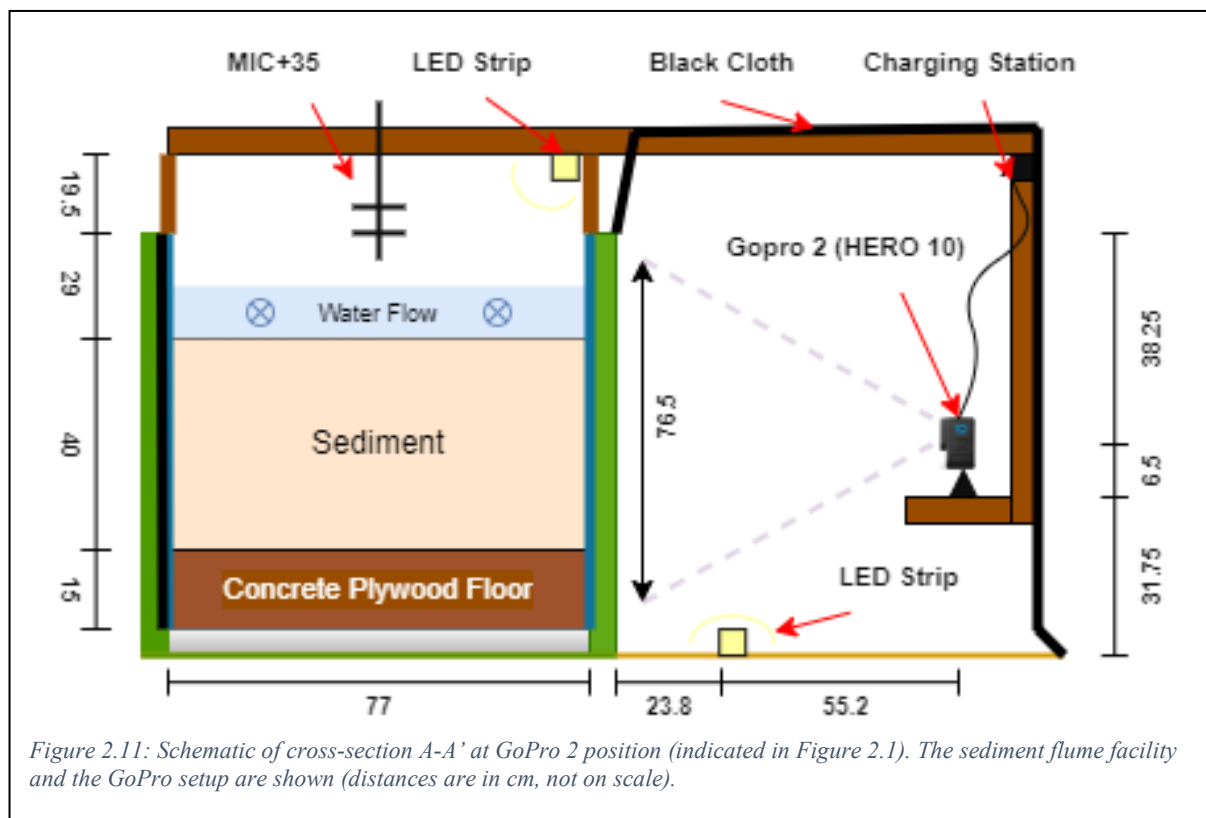


Figure 2.10: Images of the magnetostrictive position sensor, model type GH rod-style. (a) Image of the two used MPS's. The electronics housing, stroke and magnet floating ball surrounded by Styrofoam are shown. (b) Close-up image of the stabilization application on the floating ball. (c) Sketch of the sensor position and operation in the sediment flume facility.

2.2.4 GoPro Setup and Settings

The erosion process was recorded from the side of the sediment flume facility by five GoPros, Hero 10 (see Figure 2.11). They could be started simultaneously with the help of a remote control. Each GoPro was optimal positioned in front and in the middle of a plexiglass window along the sediment test layer. In this way, the five GoPros collectively observed the entire sediment packet. A frame of wooden beams and concrete plywood panels was designed and constructed to hold the five GoPros in position.



Several measures were taken to ensure an optimal visibility for further analysis, see also Figure 2.11:

- To prevent reflection in the plexiglass windows, a large tent of a black cloth was constructed around the five GoPro installations.
- The wooden beams of this tent were painted black.
- For each GoPro, a piece of black cloth was mounted against each outside plexiglass window of the left sediment flume wall.
- Two LED strips were installed, one in the sediment flume top corner, and one on the floor in front of the GoPros.
- To prevent a GoPro from running out of power during a test, black charging cables and power blocks were installed.

- Before the start of each test, the headlamps of the Hydraulic Laboratory were switched off.
- To have control over the dimensions and positions when analyzing the recordings, three measures were taken: (1) A grid was drawn on each window over the full sediment package length. This grid consisted of yellow plus markers, each 20 cm apart. Stabilized laser beams were used for constructing this grid. (2) Horizontal and vertical tape measure was taped at the window edges. (3) Chessboards were taped in the corner of a single window, one with 21 mm × 21 mm and one with 7.5 mm × 7.5 mm fields.

By downloading the phone application from GoPro, each GoPro camera could be optimally positioned separately by means of a Bluetooth connection and the clear image on the phone. The desired settings of each camera could also be set separately via this application. These settings are shown below in Table 2.1:

Table 2.1: Chosen settings of all five GoPros.

GoPro Video Settings	Video or Video Time-lapse Depending on experiment duration and available storage data
Resolution	2704 x 1520 pixels (2.7 K)
Frame Rate	60 fps (frames per second)
Field of View	L+, this setting gives no distorted straight lines
Stabilizer	Horizontal stabilizer

Remark: because of the maximum file size of 4 Gb (32 bit), the GoPro divides long duration recordings into segments of about 11 minutes, leading to separate data files for experiments lasting longer than this period.

2.3 Experimental Procedure

To perform an experiment, several actions should be taken to ensure the desired initial conditions of the setup and to guarantee proper data acquisition and storage. Figure 2.12 summarizes the 11 necessary steps. Some steps can be taken in parallel.

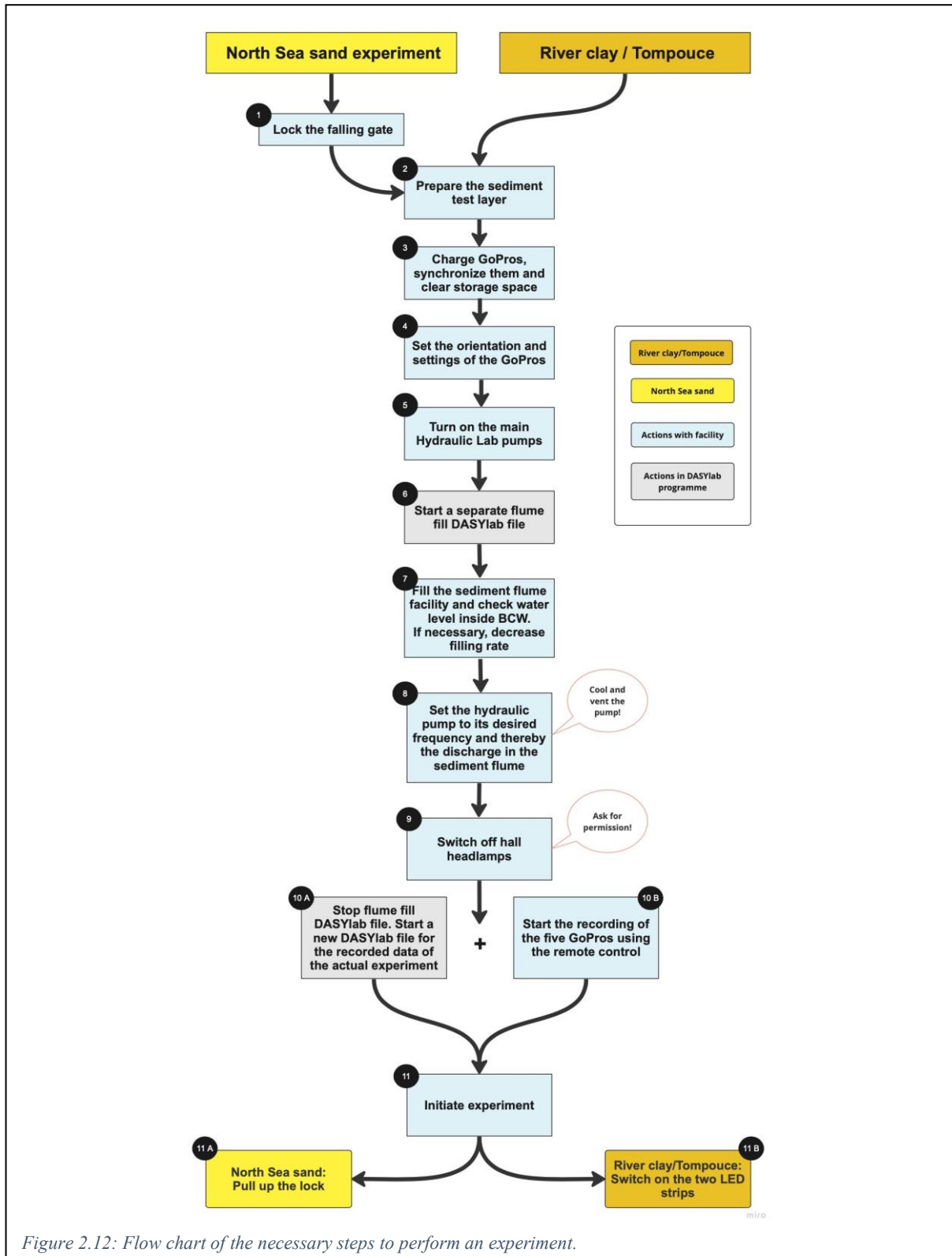


Figure 2.12: Flow chart of the necessary steps to perform an experiment.

Additional explanations for all separate steps are provided below:

1. Locking the falling gate for the North Sea sand experiments has three purposes: firstly, it creates a suitable space in the BCW for preparing the full North Sea sand package. Secondly, it prevents erosion of the sediment when the hydraulic conditions are set. Nevertheless, proper closure of the side edges of the falling gate should be checked. Lastly, it initiates a water level difference before the start of an experiment. The rectangular hole in the lock of the falling gate construction provides an overflow jet.
2. See for a detailed description of the North Sea sand, river clay and Tompouce soil preparations Sections 3.3.1, 3.3.2 and 3.3.3.
3. Precautions must be taken to ensure that all five GoPros start recording at the same time and that a single GoPro recording is not suddenly stopped during an experiment. Charging the GoPros during a long experiment can cause the GoPros to fail due to overheating.
4. The GoPros should be aimed perpendicular to the plexiglass window to minimize distortion of the image. The setting of each GoPro differs per position and per experiment. The GoPro phone application is an excellent tool to do both specifically. When everything is ready, close the entire GoPro tent with the black cloth.
5. The main reservoir is filled by switching on the main Hydraulic Lab pumps. It should be checked in advance whether there is enough water in the underground bunker.
6. A separate DASYlab file should be made and started to control the flume fill water level and set the desired flow discharge.
7. Filling the sediment flume facility to its desired water level should be done in a well-controlled manner via the upstream and downstream water inlets. These inlets can be controlled simultaneously. The cavities of the entire BCW must be filled at the same rate as outside. If this is not done carefully, air escapes with reasonable force and penetrates through the soil package. This can therefore disturb the homogeneity of the sediment test layer.
8. In order not to damage the hydraulic pump, it is necessary to aerate the pump first and then open the cooling hose.
9. Permission for switching off the headlamps must be requested from all those present in the Hydraulic Lab. This prevents a possible disruption of an ongoing experiment elsewhere in the lab.
10. For further analysis, a new DASYlab file should be named, checked and started (10 A). The GoPro phone application shows the time when a recording is started (10 B), this gives a clear time indication during an experiment.
11. When pulling up the lock, note that the resistance has increased enormously due to the water column that flows through the lock (11 A). Blinking with the LED strips is a handy (additional) method to give a time indication for further analysis (11 B).

3 Experimental Conditions

This chapter presents the experimental conditions of all experiments performed: sediment type, soil preparation methods, initial water level, setting of the pump speed and the resulting hydraulic conditions as a function of time (water levels and flow velocities). Moreover, results of extensive sediment analyses are included.

3.1 Sediment Analysis

The specifications of the two sediment types used in this study, namely North Sea sand and river clay, have been determined by sediment analysis tests. These tests were performed in the Geoscience and Engineering Laboratory of the Department of Applied Geosciences, Faculty of Civil Engineering and Geosciences at Delft University of Technology. The test procedures were based on the British Standards and the ASTM standards, which are methods of test for soils for civil engineering purposes. They contain classification tests and methods to determine the geotechnical properties. Per sediment type, the results are shown in different sections.

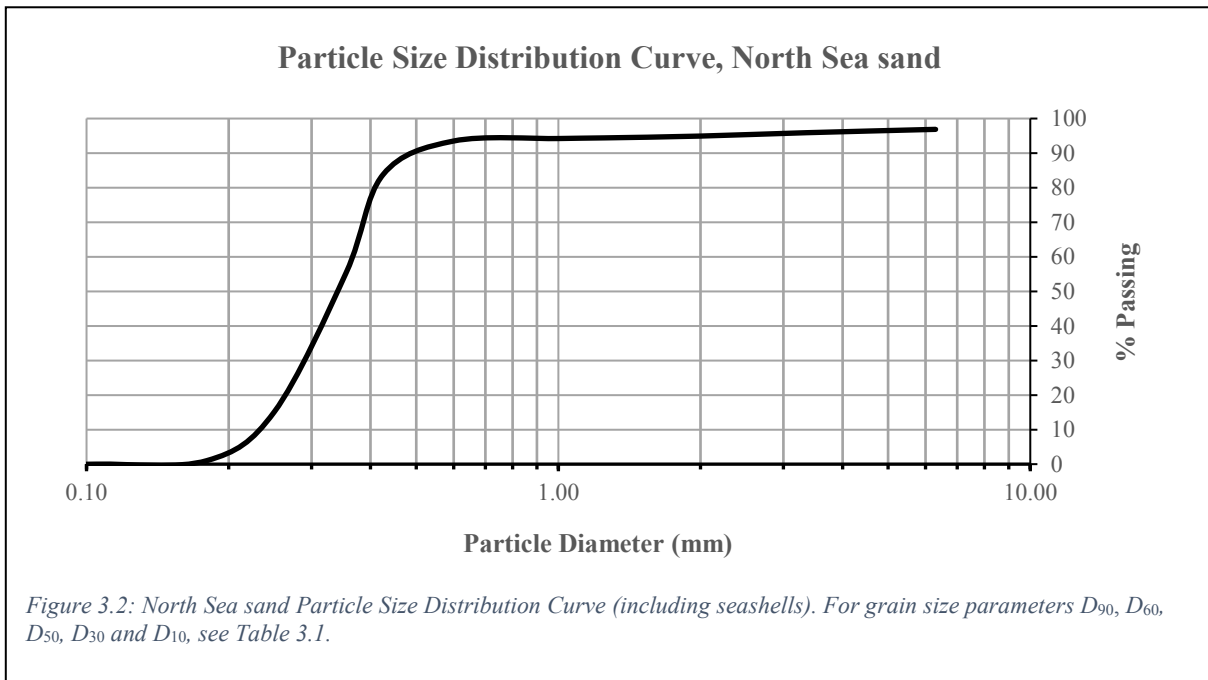
3.1.1 North Sea sand

Four identical dry sieving tests were performed in accordance with BS 1377:1975, Test 7(B). (Verwaal & Mulder, 2017). During the dry sieving tests, it was found that the North Sea sand samples contained seashells (see Figure 3.1). Their maximum size was 4 cm and the volume percentage was around 7%. The seashells have not been removed during the sediment package preparation before each experiment and may influenced the erosion process. (Cheng, et al., 2021).



Figure 3.1: Image of the remaining seashells during a dry sieving test with North Sea sand.

From the results of the dry sieving test, a particle size distribution (PSD) curve was generated (see Figure 3.2). It illustrates the amount of material that passes through each chosen sieve and the average, smallest and largest particle size (Bensoula, Missoum, & Bendani, 2014). The remaining 7% seashells have been included during the generation of the PSD curve. At the top of the curve, this is reflected in the extended horizontal plateau. The results of the North Sea sand analysis, containing the grading characteristics and coefficient values, are summarized in Table 3.1.



Five grading characteristics are indicated in the table: D_{90} , the maximum size of the smallest 90% of the sample. D_{60} , the maximum size of the smallest 60% of the sample. D_{50} , the median of the PSD curve. D_{30} , the maximum size of the smallest 30% of the sample and D_{10} , the maximum size of the smallest 10% of the sample (effective size). With the grading characteristics, a uniformity coefficient, $C_u = D_{60}/D_{10}$, of 1.63 and a coefficient of curvature, $C_c = \frac{D_{30}^2}{D_{10}D_{60}}$, of 1.014 were found. With C_u smaller than 4 and C_c between 1 and 3, the North Sea sand can be classified as a poorly graded uniform soil.

Table 3.1: Geotechnical properties of the North Sea sand.

Parameter	Symbol	Value
Sea shells percentage	%	7
Gravel percentage	%	3.1
Sand percentage	%	96.9
Fines percentage	%	0.0
90 % passing	D_{90} (mm)	0.537
60 % passing	D_{60} (mm)	0.366
50 % passing	D_{50} (mm)	0.341
30 % passing	D_{30} (mm)	0.289
10 % passing	D_{10} (mm)	0.225
Uniformity coefficient	C_u	1.63
Coefficient of curvature	C_c	1.01
Coefficient of permeability	K (mm/s)	0.32

The coefficient of permeability, K , was obtained by ir. Mario van den Berg who performed constant head tests according to the ASTM-method D2434.

3.1.2 River clay

The river clay was supplied by Boskalis and was categorized as Erosion Class 3. For an extensive categorization a sediment analysis was performed during this study. Samples were taken during the river clay package preparation, before the Tompouce experiments. Three air-tight buckets with river clay samples were filled, see Appendix A: Additional Images for pictures. For comparison, tests were performed repeatedly with the samples taken from two buckets. During the analysis period, these buckets were stored in a climate-controlled room in the Geoscience Laboratory.

A Particle Size Distribution Curve was generated by merging the results from dry sieving tests and hydrometer tests. The hydrometer tests were performed according to the BS 1377: PART 2:1990 procedure. The graphical result is illustrated below, see Figure 3.3. From this illustration, it can be noticed that the median grain size, D_{50} , of the river clay sample has a value of 0.034 mm, and therefore the soil is specified as Medium Silt (MSi).

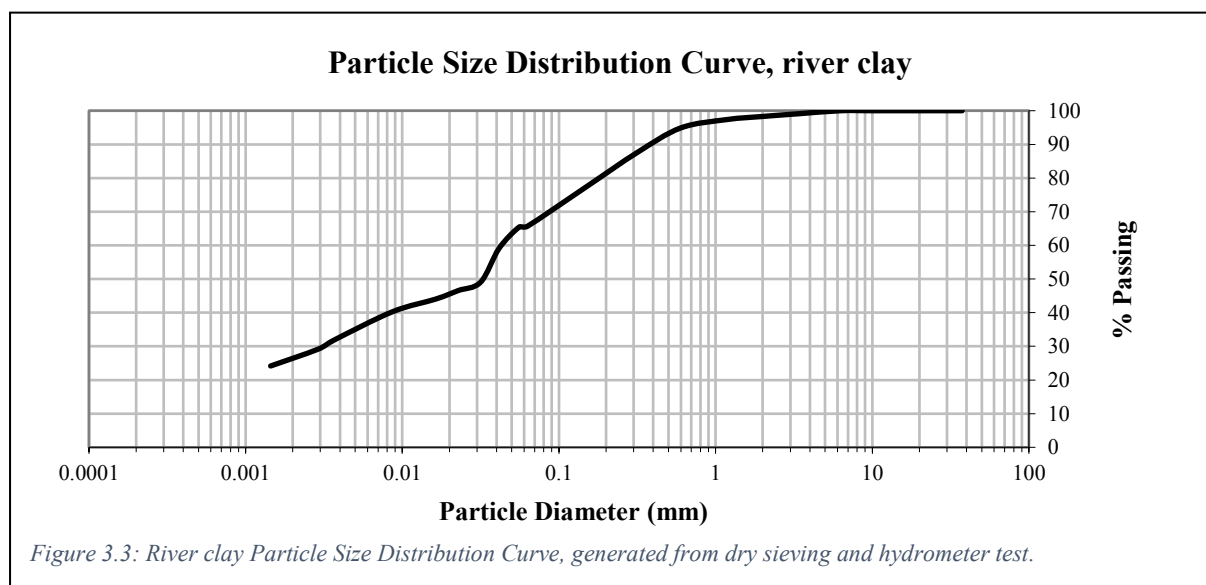


Table 3.2 gives an overview of all tested river clay classification parameters. The tests that were performed for each parameter are mentioned, together with the followed test method code. The determined parameter value presents the calculated average of repeatedly performed tests. For each parameter, their accompanying symbol and unit are provided as well.

Table 3.2: Geotechnical properties of the river clay samples. Values are averages of repeated tests.

Parameter	Symbol	Value	Unit	Test Performed	Method Code
Moisture content	w	30.86	%	Natural Moisture Content	BS 1377:PART 2,1990
Porosity	n	0.45	-	Natural Moisture content	BS 1377:PART 2,1990
In-situ density	ρ_{sw}	1.01	Mg/m^3	Density	BS 1377: Part 2:1990
Dry density	ρ_{sd}	0.77	Mg/m^3	Density	BS 1377: Part 2:1990
Liquid limit	LL	36.6	%	Fall Cone test	ISO/TS 17892-12: 2004
Plastic limit	PL	22.7	%	Rolling Method	ISO/TS 17892-12: 2004
Plasticity index	IP	13.9 (Low)	-	-	ISO/TS 17892-12: 2004
Liquidity index	IL	0.59	-	-	ISO/TS 17892-12: 2004
Consistency index	IC	0.41 (Soft)	-	-	ISO/TS 17892-12: 2004
Internal friction angle	ϕ	5.8	°	Direct Shear Test	BS 1377: part 7 1990
Cohesion	c	28.24	$kPa (kN/m^2)$	Direct Shear Test	BS 1377: part 7 1990
Undrained shear strength	c_u	36.0	$kPa (kN/m^2)$	Direct Shear Test	BS 1377: part 7 1990
Critical shear stress	τ_c	17.9	$kPa (kN/m^2)$	Direct Shear Test	BS 1377: part 7 1990

3.2 Experimental Campaign

In total, twelve experiments were performed within this study. North Sea sand was tested in the first three experiments. After the third run, it became clear that the results obtained were sufficient for further analysis. After these North Sea sand experiments, nine experiments were performed with river clay, until this sediment package was eroded away almost completely. Six experiments in normal conditions and three with the Tompouce setup. Table 3.3 provides an overview of the essential information of every experiment.

The *first* column in Table 3.3 lists the serial ID number per experimental type: NSS1-3, RC1-6 and TP1-3 presenting the North Sea sand, river clay and Tompouce experiments respectively. These codes will from now on be used for experiment designation in this report.

The *second* column shows the duration of each experiment in hours:minutes:seconds. The duration was determined by the time between when the desired flow discharge of the hydraulic pump was set, and when the pump was switched off. The pump was switched off for three reasons, resulting in differences in duration between experimental type and between single experiments. Firstly, when the sediment package was completely eroded away. This only

happened during the North Sea sand experiments. Secondly, when no discernible erosion mechanism was observed, not even after changing the hydraulic condition (occurred during river clay and Tompouce experiments). Lastly, when a defect occurred with one of the GoPros. The *third* column presents the averaged measured water level, H , in cm relative to the sediment flume facility bottom after the flume was completely filled to the desired level. For all North Sea sand experiments, H was kept constant. After river clay experiment RC2, H was reduced. This was done to try and get an aerated overflow jet during the experiment. Per Tompouce experiment, H was increased to achieve a more intense overflow jet, resulting in more intense headcut erosion due to undermining during the experiment.

The *fourth* column gives the maximum crest flow velocity, $U_{c,max}$, measured by the EMS in m/s during an experiment.

The *fifth* column gives the maximum flow discharge, $Q_{m,max}$, as measured by the PPF sensor in l/s. For comparison, the theoretical maximum flow discharge, $Q_{e,max}$, in l/s has been estimated using Equation 3.1 (see also (Badr & Mowla, 2014), (Chanson & Eraso, 2004) and (Osman Akan & Iyer, 2021)):

$$Q_{e,max} = C_d \left(\frac{2}{3}\right)^{\frac{3}{2}} \sqrt{g} W h_0^{\frac{3}{2}} \quad (3.1)$$

With acceleration of gravity, g (m/s²), sediment flume facility width, W (0.77 m), the overflow head upstream of the weir, h_0 (m) – see also Figure 2.2 – and dimensionless discharge coefficient, C_d . Due to the smooth transition of the slope upstream of the weir, C_d could be set to 1.

The *last* column provides some additional notes.

All data of *all* experiments are available for further analysis and can be found in the 4TU.ResearchData Repository. For details of the filenames see Appendix C: Available Data.

The stability of foreland types under dike breach conditions – an experimental study

Table 3.3: Overview of the twelve experiments performed. Division is made per experimental type: North Sea sand (3 experiments), river clay (6 experiments) and Tompouce (3 experiments). The test duration (hh:mm:ss), flume fill water level H (cm), the maximum crest flow velocity $U_{c,max}$ (m/s), the measured maximum flow discharge $Q_{m,max}$ (l/s) and estimated maximum flow discharge $Q_{e,max}$ (l/s) are shown. Some additional notes are also provided. ⁽¹⁾ unreliable measured value.

	Test Duration (hh:mm:ss)	Flume Fill Water Level, H (cm)	Maximum Crest Flow Velocity, $U_{c,max}$ (m/s)	Measured Maximum Flow Discharge, $Q_{m,max}$ (l/s)	Estimated Maximum Flow Discharge, $Q_{e,max}$ (l/s)	Notes
<u>North Sea sand</u>						
NSS1	00:04:35	62	1.3	148	154	Falling gate used. Interference hydraulic jump
NSS2	00:03:21	63	1.5	201	217	Falling gate used. Interference hydraulic jump
NSS3	00:03:37	62	1.7	299⁽¹⁾	262	Falling gate used. Lots of sediment in system, Q_m unreliable
<u>river clay</u>						
RC1	00:09:21	65	1.4	256	252	Start river clay experiments. Falling gate used
RC2	00:14:54	65	1.5	249	249	Preparation new initial headcut. Continued from RC1 headcut final position (at flume window 2).
RC3	00:26:00	50	1.2	127	129	Continued from RC2 headcut final position (at flume window 2).
RC4	00:42:00	48	1.1	96.3	101	Continued from TP3 headcut final position (between flume window 3 and 4).
RC5	01:55:00	48	1.4	180	190	Preparation new initial headcut. Continued from RC4 headcut final position (at flume window 4).
RC6	00:48:00	49	1.5	190	194	Final river clay experiment. Preparation new initial headcut. Continued from RC5 headcut final position (at flume window 4).
<u>Tompouce</u>						
TP1	00:44:00	44	1.0	125	134	Preparation Tompouce setup and new initial headcut. Continued from RC3 headcut final position (at flume window 3).
TP2	00:55:00	51	0.9	78.1	83	Preparation new Tompouce setup and initial headcut. Continued from TP1 headcut final position (at flume window 3).
TP3	01:34:00	65	1.4	248	256	Final Tompouce experiment. Continued from TP2 headcut final position (at flume window 3).

The headcut during the river clay experiments had no sharp edge. This made it difficult to realize an aerated nappe, which was later fixed by the Tompouce setup. For each new river clay experiment, a desired flow discharge must be set repeatedly. During the river clay and Tompouce experiments, the flow discharge was adjusted in combination with the initial flume fill water level per experiment in order to obtain the desired hydraulic conditions.

The erosion process during the first two North Sea sand experiments, NSS1 and NSS2, was disturbed by interference of the hydraulic jump. After the start of the experiment a hydraulic jump occurred downstream, moving rapidly towards the already lowered falling gate. After reaching the falling gate construction this resulted in irregular uplifting of the gate. This undesired effect was prevented by increasing the flow discharge and did not occur in experiment NSS3. Nevertheless, the data obtained during NSS1 and NSS2 might be useful for further studies.

After the North Sea sand experiments, the river clay package was installed. Three experiments were performed successively: RC1-3.

At RC1, the clay package extended until the falling gate construction (7 m). However, lowering the gate to initiate the experiment resulted in tearing apart of the headcut. This created a cascading headcut. After 9 minutes, the headcut was smoothed by mass surface erosion and no more erosion was observed, so the experiment was stopped.

At RC2 the headcut was newly prepared approximately one meter upstream the falling gate. During this experiment, an attempt was made to maintain the same hydraulic conditions that prevailed in experiment RC1. Unfortunately, the hydraulic conditions were unfavorable for aerated nappe formation. That is why at RC3 the hydraulic conditions were adjusted until an aerated nappe occurred.

Thereafter, three Tompouce experiments were performed: TP1-3. Before experiments TP1 and TP2, the concrete plywood top panel was cut at the position of the newly prepared headcut. No adjustments were made before experiment TP3, because this experiment was performed right after experiment TP2. The maximum flow discharge and flume fill water level was changed to influence the nappe formation and downstream water level during an experiment.

Finally, the measurement campaign was concluded by three additional clay experiments: RC4-6, until most of the sediment package was washed away. Unfortunately, during these experiments there was a lot of trouble with clay pieces sticking to the sediment flume glass wall near the headcut, which greatly hindered the observations. In addition, the observations during experiment RC4 were made more difficult because the headcut was located between two observation windows.

Experiments NSS3, RC3 and TP2 were performed successfully and will be analyzed and discussed further in the following sections. Section 3.3 provides the experimental conditions of these three experiments in more detail. The results will be shown in the next chapter.

3.3 Soil and Hydraulic Conditions for Experiments NSS3, RC3 and TP2

In this section, the experimental conditions of the experiments NSS3, RC3 and TP2 are described to support the further analysis in this report. For each experiment, the preparation of the sediment package will be explained, after which the hydraulic conditions will be illustrated using graphs. The hydraulic conditions were measured by the discharge sensor, the flow velocity sensor (EMS) and the water level sensors (MIC and MPS), as described in Section 2.2. The graphs of the water levels are ordered in streamwise direction (h_{1-5}).

3.3.1 Experiment NSS3

Soil Preparation

The North Sea sand required no preparation outside the sediment flume and could therefore be poured directly when the falling gate was closed. The following essential preparations were made:

- Glass and non-sedimentary material were removed by hand, to avoid their influence on the erosion process.
- Several times the sand package was walked over to allow consolidation to take place with the aid of human weight.
- To prevent irregularities in the top layer, which will grow during the test, it was smoothed as accurately as possible.

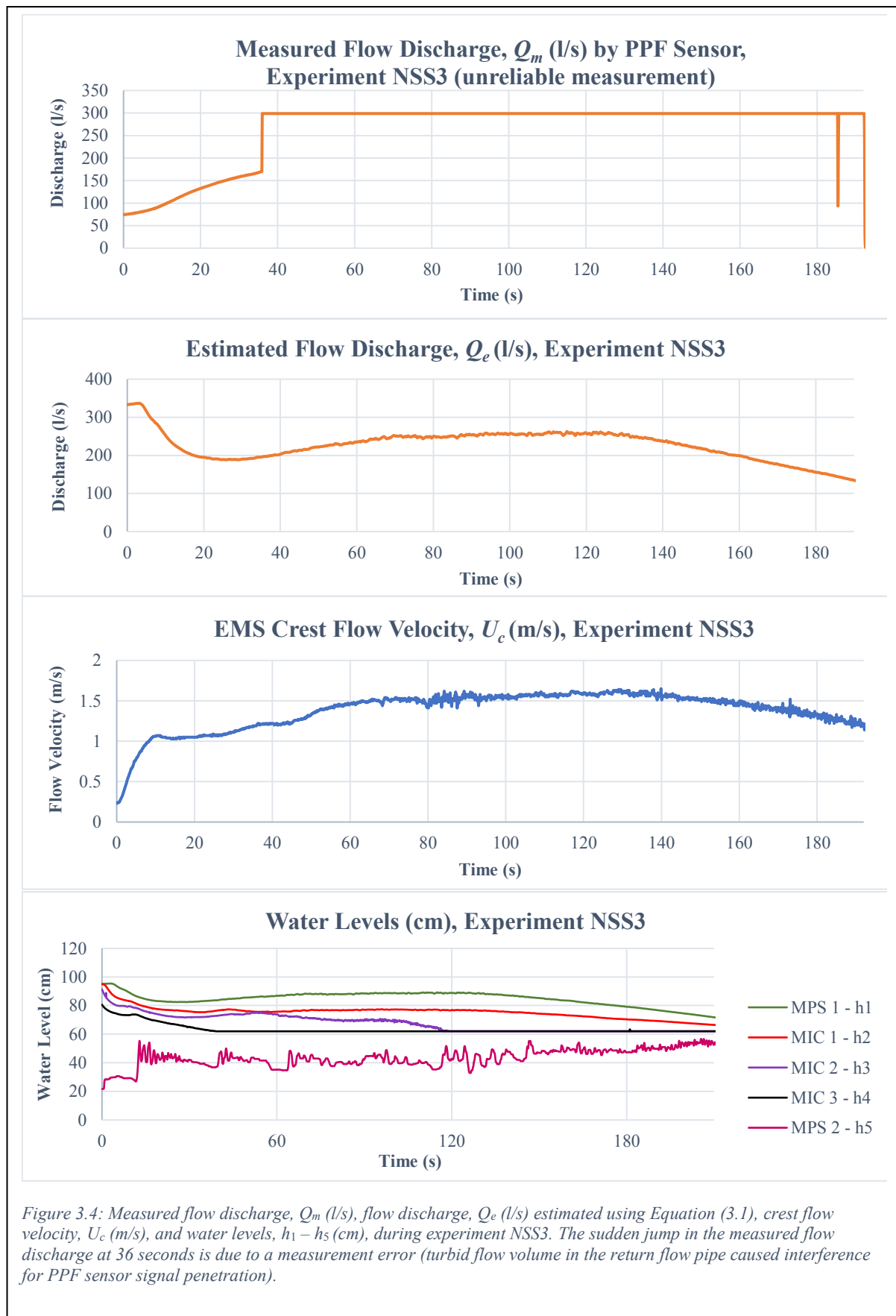
Hydraulic Conditions

Figure 3.4 shows a graphical representation of the hydraulic conditions during test NSS3, measured by the 7 measuring instruments. Three peculiarities can be observed: Firstly, a sudden jump at 36 seconds in the first graph, presenting the pump discharge measurement. The jump is probably a measurement error, most likely caused by turbidity, which prevents the signal from the PPF sensor to properly penetrate the flow volume. This turbidity arose because sediment from previous experiments (NSS1 and NSS2) had settled in the return flow pipe. Fortunately, this undesired effect did not appear at the measurements with clay.

Secondly, the intensive turbulent behavior of the water level measured by the MPS 2, which is located downstream. This is due to high flow velocities during the test.

Lastly, the graphs of water level sensors MIC 3 and MIC 2 continue horizontally from 35 seconds and 110 seconds respectively. After these specific moments, the water level was outside the 65 cm detection zone of the sensors. This has been observed by GoPro's recordings and verified.

To obtain an estimate of the flow discharge, Q_e , Equation (3.1) was applied. The upstream energy head, h_0 , was obtained by subtracting the weir height, p in Figure 2.2, from h_1 , as measured by MPS 1. The result is given in the second graph of Figure 3.4. Of course, Equation (3.1) is not valid at the start of the measurement, when the flow accelerates and must develop to a quasi-steady state.



3.3.2 Experiment RC3

Soil Preparations

Much attention was paid, and many attributes were used to prepare the 2.5 m³ soil of the sediment test layer in the right condition. Heavy gear, such as shovels, rakes, hammers and axes were used to pulverize and transfer the sediment from the large transport bags into the sediment flume facility. A vibrating needle, water nozzles, air blowers, elements for consolidation were applied to get the soil test layer in the desired condition. The river clay was delivered by Boskalis in Big Bags of 1.5 m³. These bags contained very dense dry clay chunks with a diameter of around 50 cm. Outside the sediment flume, these chunks were manually reduced to a diameter of 10 cm with the attributes mentioned above. During this process, the boulders found were removed by hand as much as possible. Figure 3.5 shows a photo to give an impression of the size of the boulders found and removed.



Figure 3.5: Image of boulders found and removed during River clay preparation process, scale in cm.

The river clay package was built up in 4 layers of 10 cm on top of the false bottom. Each layer was made homogeneous by a combination of intensive mixing, evenly moistening with water and the use of a vibrating needle. The entire sediment package was consolidated for a few days by repeatedly spreading human weight over the top layer. After a drying period of two weeks, some cracks appeared in the sediment top layer. These cracks turned out to be crucial in the erosion process later in this study. Before the experiments were performed, the location and width of the 10 main cracks were identified using codes (S1-S10). On the outside of each GoPro observation window, each code was pasted at the respective crack location for further analysis. To give a clear impression, some pictures of the drying period, the crack formation and codes are shown below in Figure 3.6 and Figure 3.7.

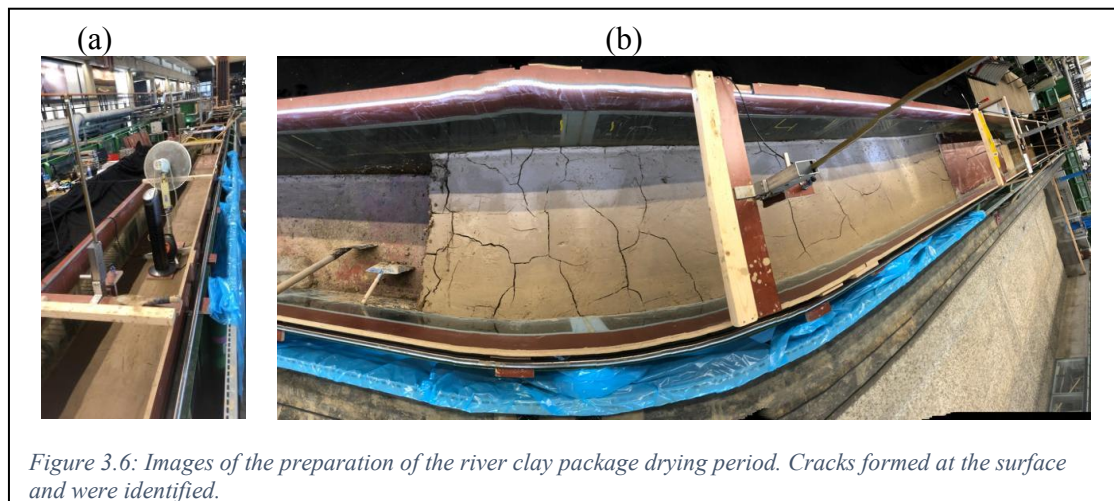


Figure 3.6: Images of the preparation of the river clay package drying period. Cracks formed at the surface and were identified.

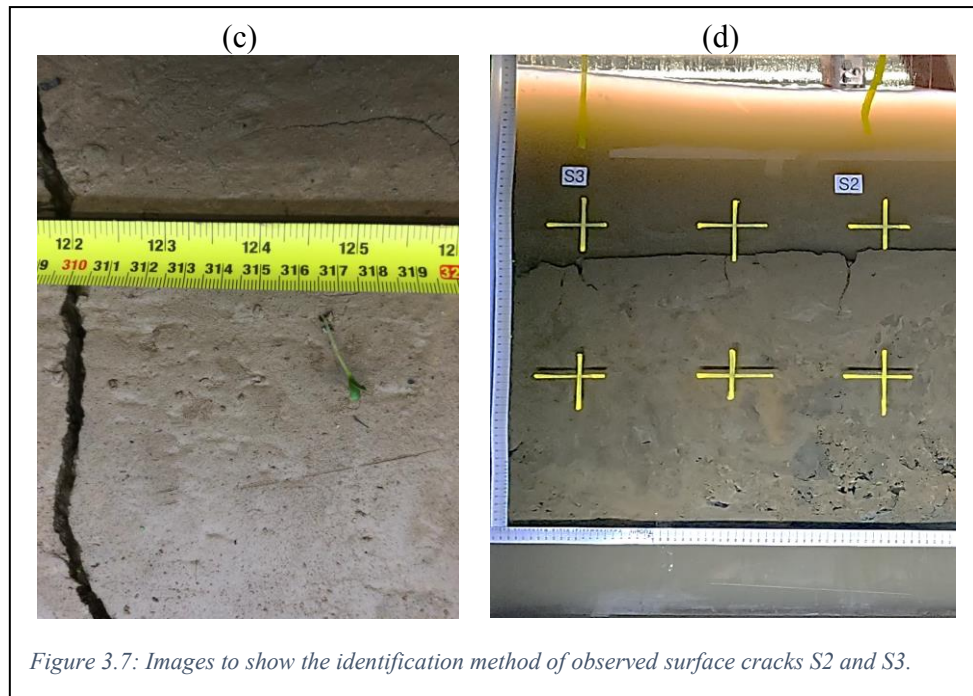


Figure 3.7: Images to show the identification method of observed surface cracks S2 and S3.

Hydraulic Conditions

Figure 3.8 shows a graphical representation of the hydraulic conditions during test RC3, measured by the 7 measuring instruments. As can be seen, the pump discharge, Q , was increased step by step during this experiment. This was done to create an aerated nappe and to amplify certain erosional mechanisms.

Please note the excellent agreement between the measured flow discharge and the estimated flow discharge (Q_m and Q_e , respectively).

Due to the previous trials RC1 and RC2, the headcut had already migrated past the location of MIC 3. As a result, the water level to be measured (h_4) for test RC3 fell outside the range of sensor MIC 3 and is therefore omitted.

Note that during the first 5 minutes of the test, with a low flow discharge value, the EMS probe was outside the water column and gave therefore erroneous results.

Unfortunately, this could not be guaranteed during certain experiments due to low water levels and therefore, occasionally, some errors occurred in the measurements.

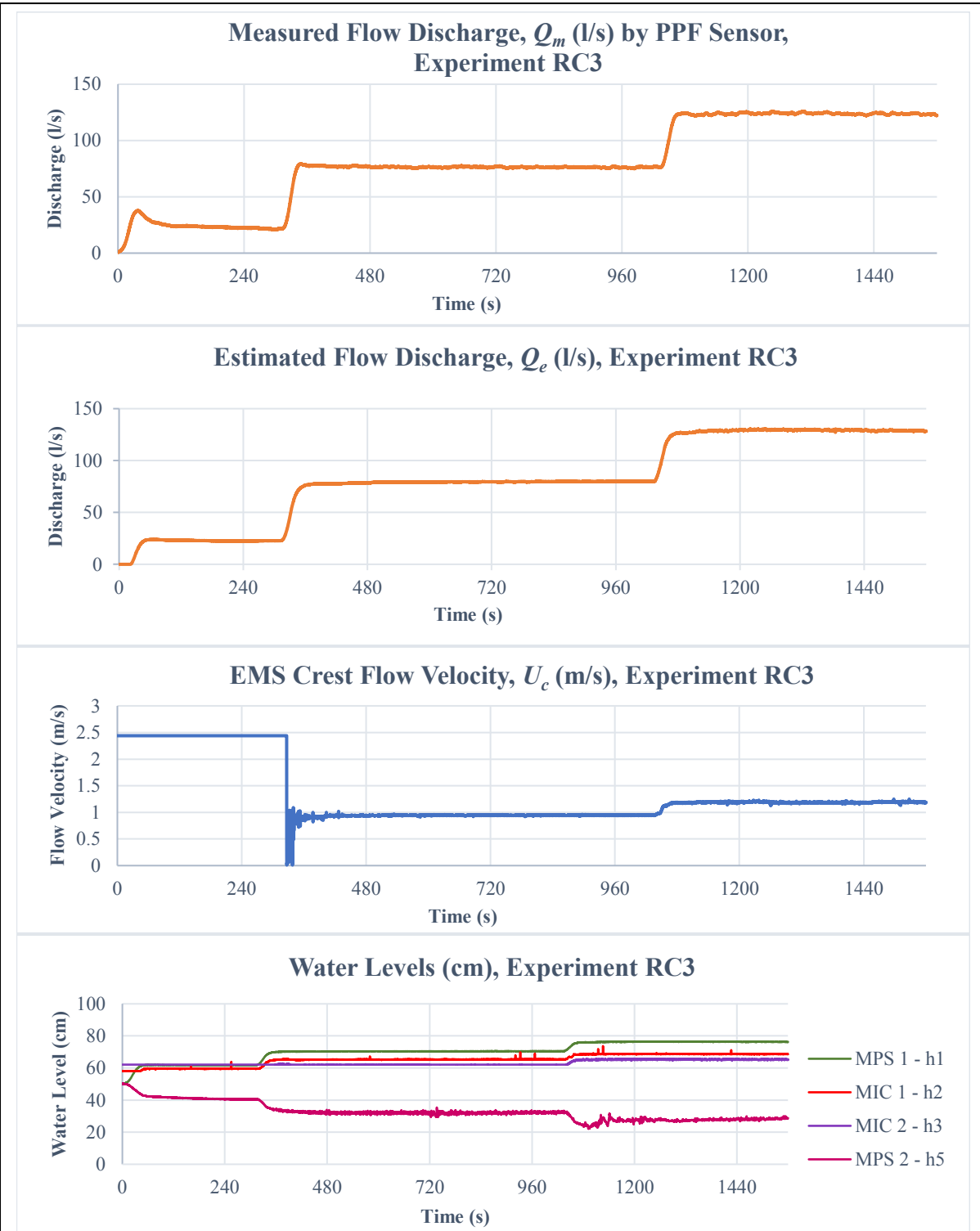


Figure 3.8: Measured flow discharge, Q_m (l/s), flow discharge, Q_e (l/s) estimated using Equation (3.1), crest flow velocity, U_c (m/s), and water levels, $h_1 - h_3$ and h_5 (cm), during river clay experiment RC3.

3.3.3 Experiment TP2

Soil Preparations

See Section 2.1.1 for the overall description of the Tompouce experimental setup. Before the concrete plywood top edge was constructed, the headcut was carefully cut at the desired distance. Careful, in the sense that the headcut face was influenced as little as possible by pressing, kneading, and molding.

The concrete plywood top layer was attached with connections along the plexiglass. These connections were smoothed to minimize disturbance of the flow as much as possible.

Hydraulic Conditions

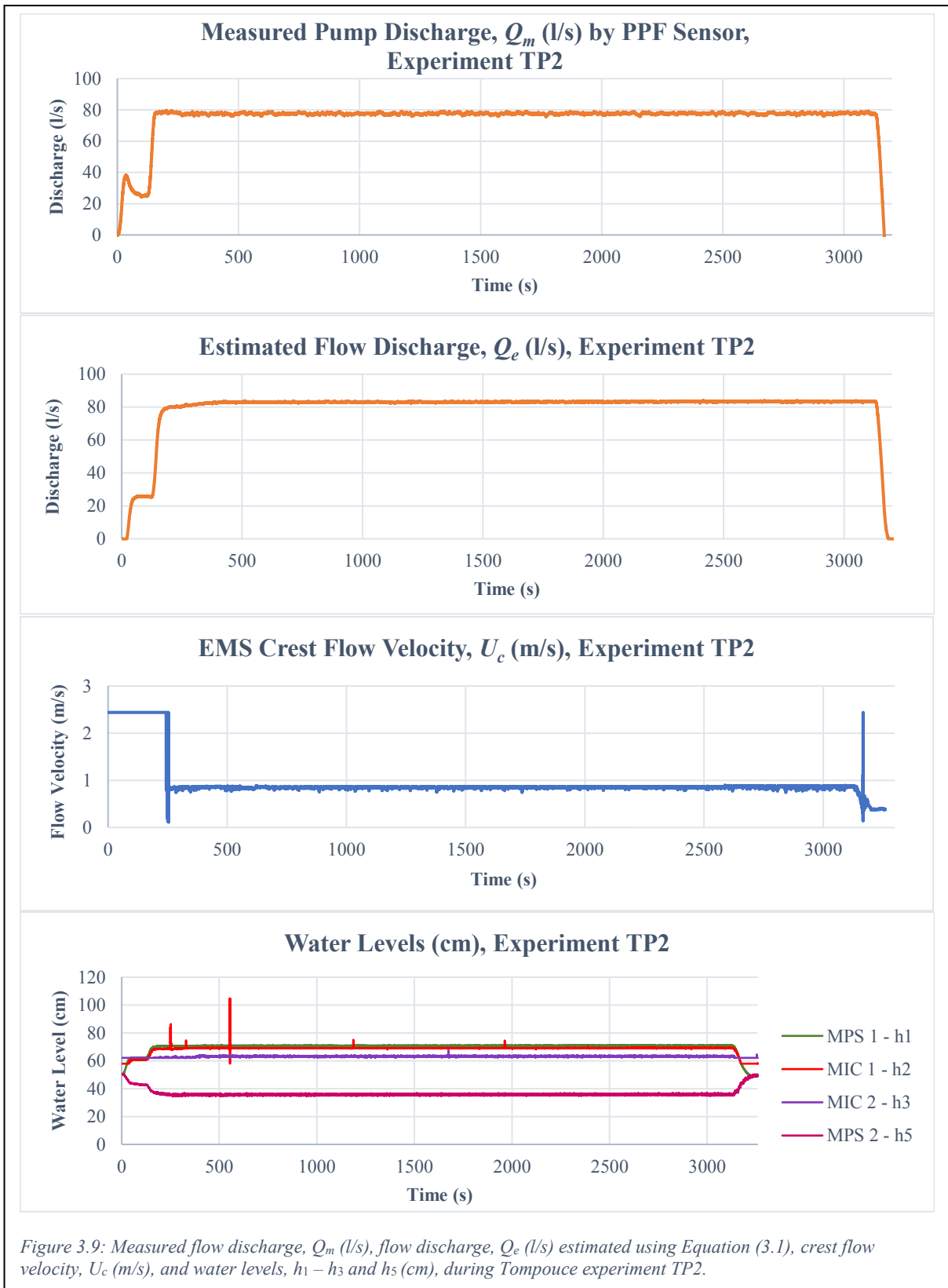
Figure 3.9 shows a graphical representation of the hydraulic conditions during test TP2, measured by the 7 measuring instruments. As can be seen, the pump discharge was kept constant at 78 l/s.

Again, the measured flow discharge and the estimated flow discharge (Q_m and Q_e , respectively) agree very well. This gives confidence in the estimated flow discharge for experiment NSS3, where the measured value was unreliable.

Due to the previous river clay experiments, the headcut had already migrated past the location of MIC 3. As a result, the water level to be measured for test RC3 fell outside the range of MIC 3 and is therefore omitted.

Note that during the first 4 minutes of the test, with a low discharge value, the EMS probe was outside the water column and gave therefore erroneous results.

A hydraulic jump occurred in between MIC 1 and MIC 2; therefore, the turbulence at the position of MIC 2 was strongly intensified.



4 Experimental Results and Observations

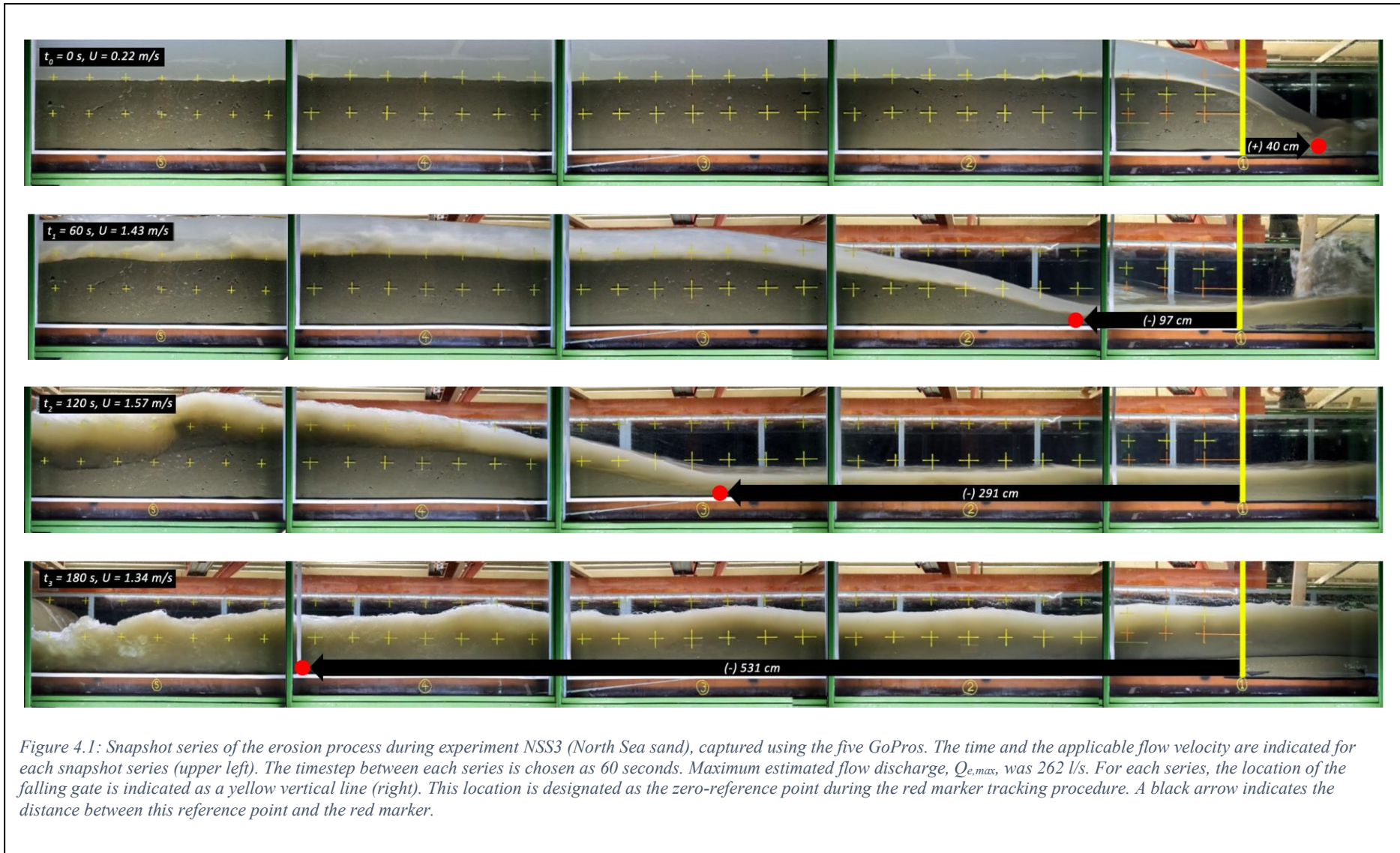
This chapter presents the results of the experiments NSS3 (North Sea sand), RC3 (river clay) and TP2 (Tompouce). Specific observations are included per experiment.

4.1 Results of Experiment NSS3

By combining the five GoPro recordings of experiment NSS3, the erosion process was captured as four snapshot series (see Figure 4.1). The time (t_0 until t_3), and applicable flow velocity are indicated for each snapshot series. The timestep between each series is chosen as 60 seconds. It appeared to be difficult to track the headcut foot automatically with numerical methods, such as Canny Edge Detection (Lohithaswa, 2015). This is due to the turbulent water conditions, the water column becoming more and more turbid and the soil adhering to the plexiglass windows. Therefore, the change of the x-position of the headcut foot is chosen as measure for the migration rate, since this position can be easily determined manually from the GoPro recording. A red marker is sketched in each snapshot series to indicate the location of the headcut foot. The yellow vertical line indicates the location of the falling gate and serves as a zero-reference point during the red marker tracking procedure. A black arrow indicates the distance between this reference point and the red marker. Notice that at time t_0 , the red marker is 40 cm to the right (downstream) of the yellow vertical line. At the start of the experiment, the 40 cm high headcut became unstable when it became detached from the falling gate and fell forward, downstream. This extra distance is included in the determination of the red marker distance and the migration rate.

Two graphs are provided which show the red marker x-position and migration rate as a function of time (see Figure 4.2 and Figure 4.3). In order to make these graphs, the red marker was tracked every 30 seconds. The secondary y-axis presents the measured EMS crest flow velocity, U_c , during experiment NSS3.

For the description of the soil preparation and hydraulic conditions of experiment NSS3, see Section 3.3.1.



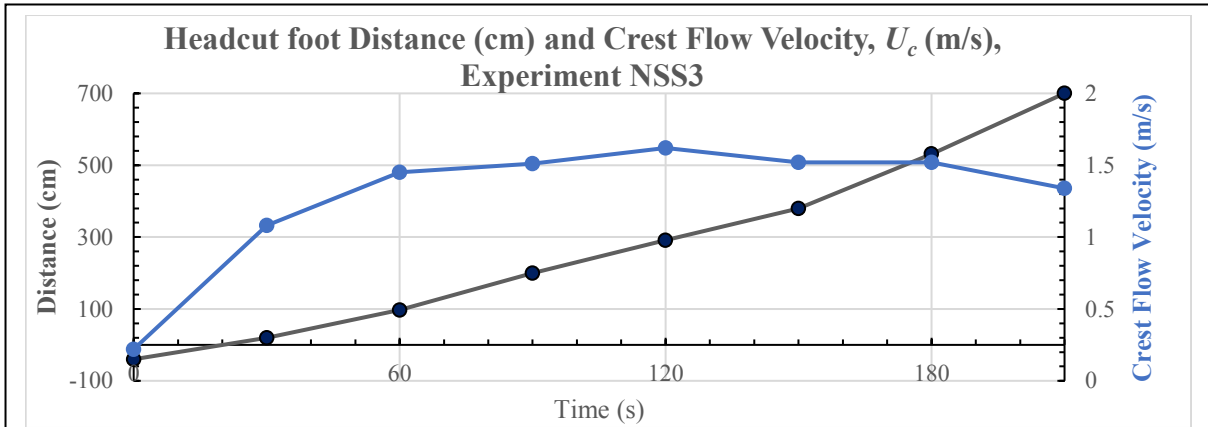


Figure 4.2: Tracked x -position of the headcut foot (the red marker in Figure 4.1) as a function of time during experiment NSS3 (North Sea sand) (black). The second y -axis presents the measured crest flow velocity, U_c (blue).

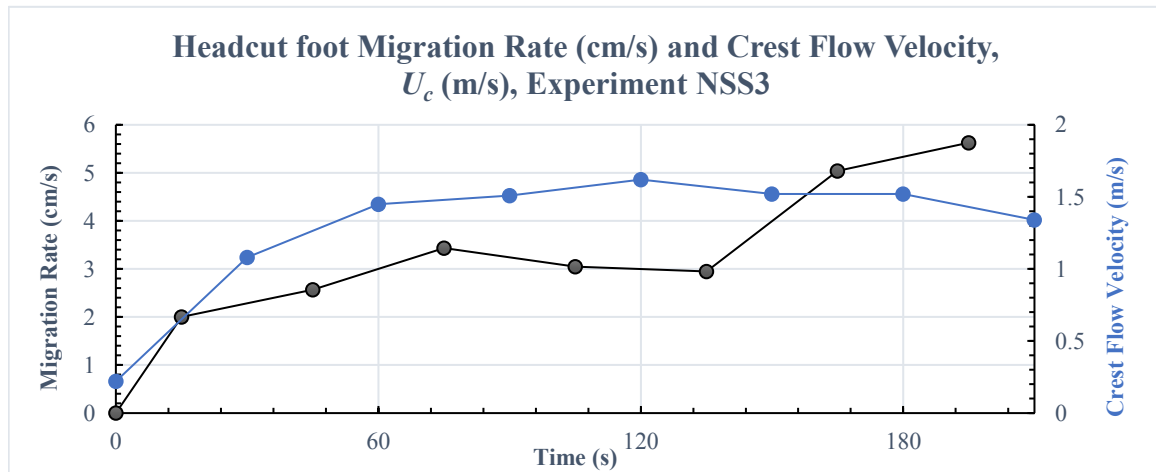


Figure 4.3: Headcut foot migration rate during experiment NSS3 (North-Sea sand) (black). The second y -axis presents the measured crest flow velocity, U_c (blue).

4.2 Observations of Experiment NSS3

During experiment NSS3, some interesting phenomena were observed and can also be seen in the snapshot series in Figure 4.1. After the falling gate was released, the headcut front quickly eroded to its angle of internal friction and surface erosion takes place over the full sediment package. The flow was accelerated over the slope and local erosion increased as a result. This led to the slope migrating further upstream under its critical angle. From the start of the experiment, a scour hole formed immediately after the concrete plywood section of the BCW ramp. The cause of this scour hole formation is due to the surface roughness transition from the (smooth) concrete plywood to the sediment package, which causes a change in the bed shear stress. Due to this scour formation (erosion) and the erosion of the headcut front during the experiment, the circulated water flow became accumulated with suspended sediment and became more turbid (see also the third and fourth snapshot series). This decreased the transport

capacity of the water column. If this scour formation could be prevented, the top layer would continue to erode to the concrete plywood edge of the broad-crested weir under the aforementioned angle of internal friction.

From the graphs in Figure 4.2 and Figure 4.3 the following can be noticed:

- In the first 80 seconds, the migration rate increased up to a rate of approximately 3 cm/s, due to the increasing flow discharge.
- After 80 seconds, the migration rate decreased. This is due to the above-mentioned decrease of the water column transport capacity.
- At 160 seconds, the erosion processes of the scour hole and headcut front met, which amplified the erosion rate. This can be seen by an increase in migration rate.

4.3 Results of Experiment RC3

This section shows the results of test RC3, which had a duration of 26 minutes (see Table 3.3). At the start of this experiment, the river clay headcut had migrated past halfway window 2, in front of GoPro 2 (see Figure 2.1). This was due to erosion during the previous experiments (RC1 and RC2). Remarkably, the river clay erosion was caused by a completely different mechanisms than was the case with the sand erosion, which was discussed in the previous section. Here, crack formation, mass and headcut erosion are observed. In order to visualize these important mechanisms, several snapshots of video file *GP_2_RClay_3.2* (see also Appendix C: Available Data C: Available Data), are made, included and discussed further on. Nine snapshots are produced to provide a clear impression. The brightness and color contrast are edited to improve the visibility. The pump discharge was kept constant between the first and last snapshot (t_9).

The first snapshot (Figure 4.4) was taken at $t = 450$ seconds. The yellow plusses are 20 cm apart (both horizontally and vertically). S2 and S3 indicate the actual positions of the second and third observed surface cracks from the headcut (See Section 3.3.2). At this moment, the headcut has already eroded beyond crack S2, and crack S3 starts to grow. A red circle marks the location of crack S3 and is the focus point for further analyses.

The eight follow-up snapshots (until $t = 780$ s) (Figure 4.5 till Figure 4.13) show 5 foreland erosion phenomena: (1) the growth of crack S3, (2) the erosion at the base of the headcut due to undermining, (3) the block sliding- and rotational failure mechanism, (4) the formation of a non-aerated nappe after the block residue is washed away and (5) the formation of a new crack in the top layer (repeating the headcut block erosion process). Note the differences in time steps between each phenomenon.

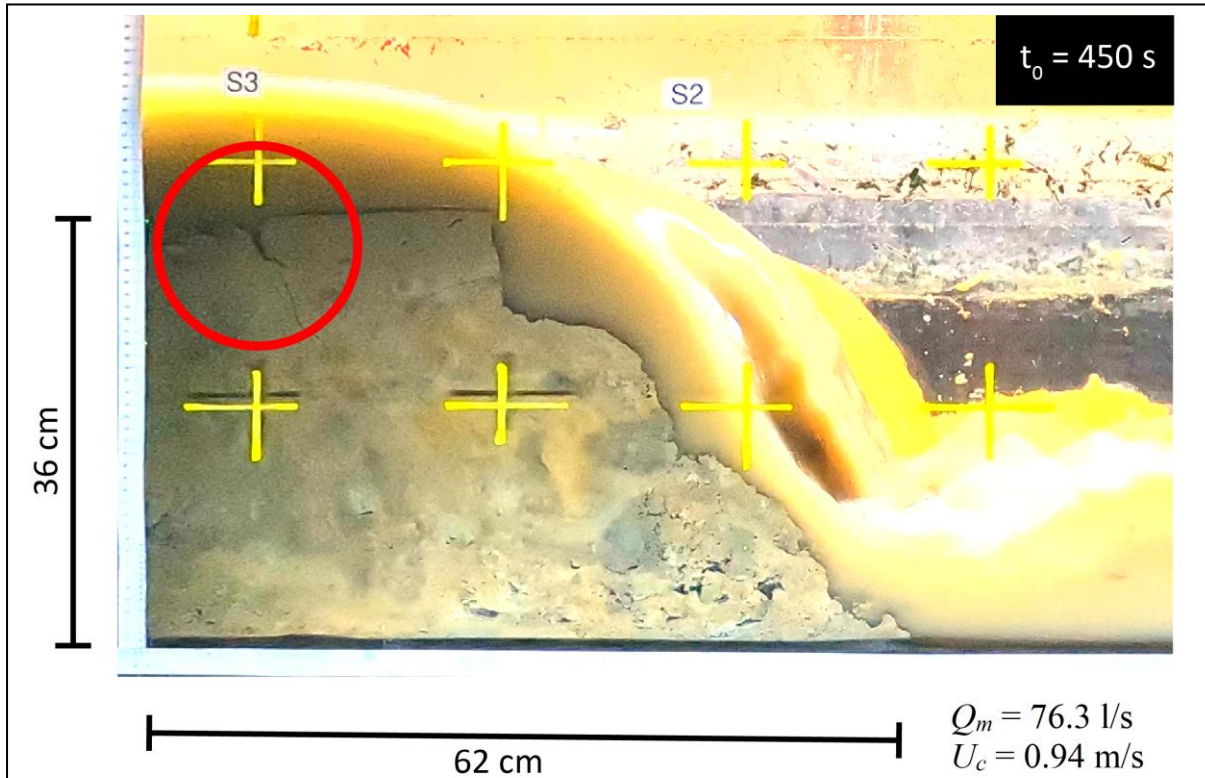


Figure 4.4: Modified GoPro snapshot during experiment RC3 at time $t_0 = 450$ seconds. Hydraulic conditions: measured flow discharge, $Q_m = 76 \text{ l/s}$ and crest flow velocity, $U_c = 0.94 \text{ m/s}$. Dimensions of the river clay section are 62 cm horizontal and 36 cm vertical. S2 and S3 indicate location of the identified surface cracks formed during soil preparation phase. The red circle indicates observed initial crack formation.

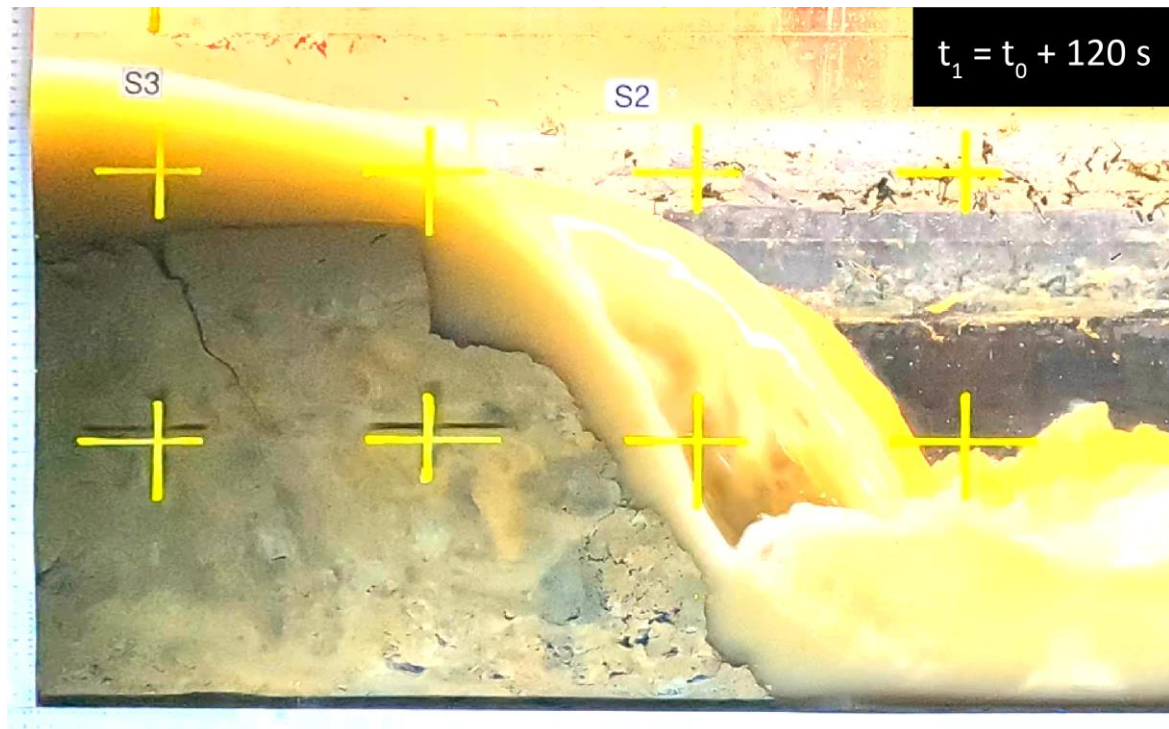


Figure 4.5: RC3 GoPro 2 snapshot at $t_1 = t_0 + 120$ seconds (2 minutes). Crack S3 formation grows due to increasing shear stress.

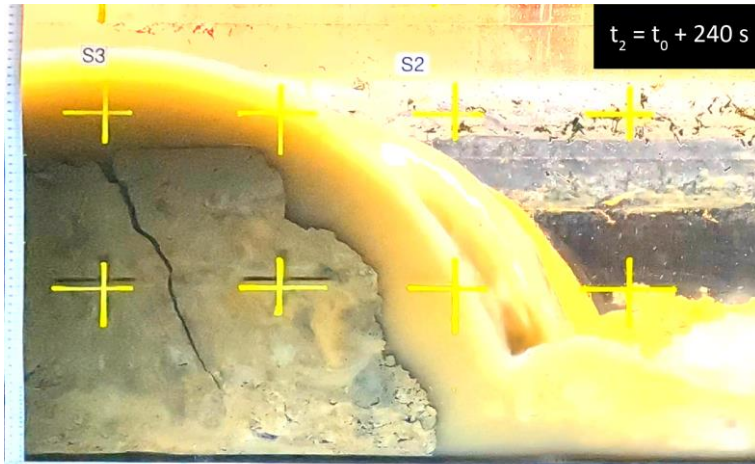


Figure 4.6: RC3 GoPro 2 snapshot at $t_2 = t_0 + 240$ seconds (4 minutes). Further growth of crack S3 formation due to increasing shear stress.

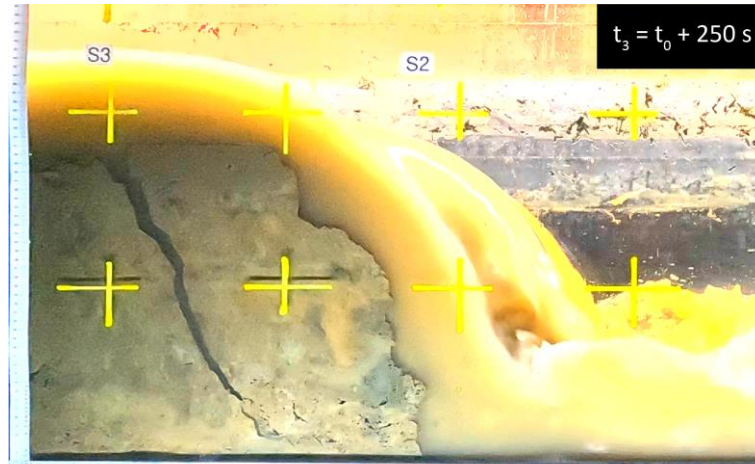


Figure 4.7: RC3 GoPro 2 snapshot at $t_3 = t_0 + 250$ seconds ($t_2 + 1$ second). Start of sliding block failure mechanism.

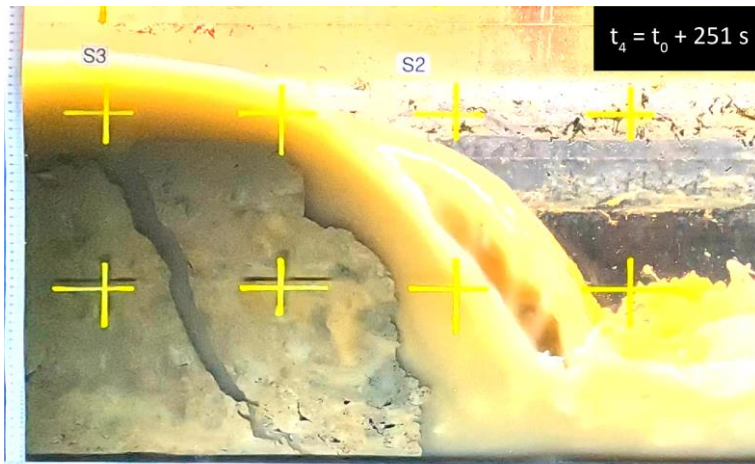


Figure 4.8: RC3 GoPro 2 snapshot at $t_4 = t_0 + 251$ seconds ($t_3 + 1$ second). Further advancement of sliding and rotational block failure mechanism.

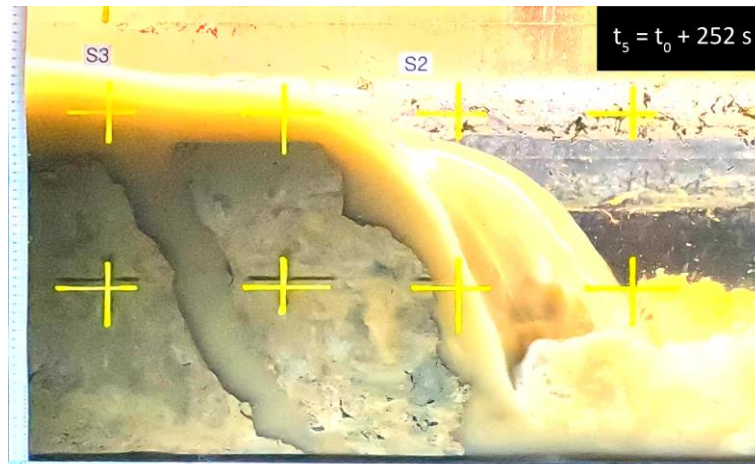


Figure 4.9: RC3 GoPro 2 snapshot at $t_5 = t_0 + 252$ seconds ($t_4 + 1$ second). Last moment before the eroded block is pushed away.



Figure 4.10: RC3 GoPro 2 snapshot at $t_6 = t_0 + 253$ seconds ($t_5 + 1$ second). The block has become completely detached and is pushed further downstream by impulses of water flow.



Figure 4.11: RC3 GoPro 2 snapshot at $t_7 = t_0 + 254$ seconds ($t_6 + 1$ second). The eroded block has been pushed one meter downstream. The downstream water level increases and an aerated nappe arises at the newly formed headcut.



Figure 4.12: RC3 GoPro 2 snapshot at $t_8 = t_0 + 290$ seconds ($t_7 + 36$ seconds). During this time headcut erosion occurred. The eroded block is washed away and therefore the downstream water level decreases. A new crack formation is indicated with the red circle. The block erosion process repeats.

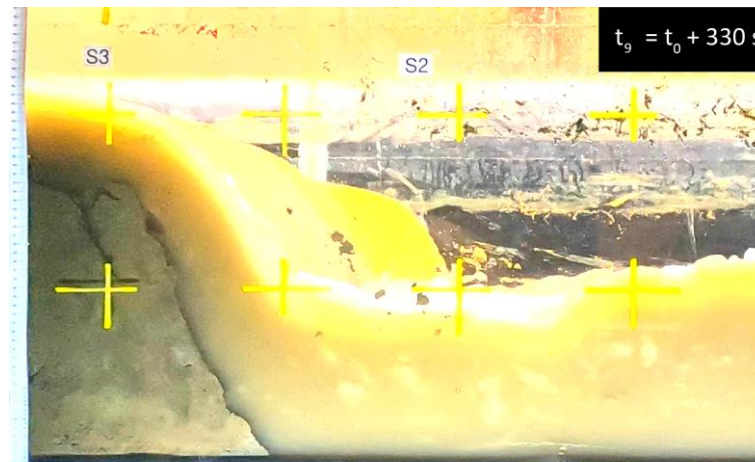
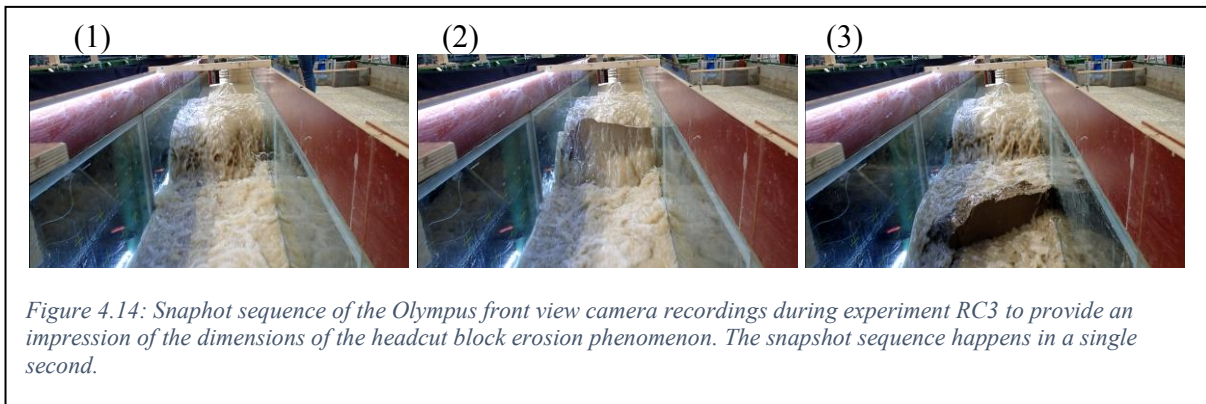


Figure 4.13: RC3 GoPro 2 snapshot at $t_9 = t_0 + 330$ seconds ($t_8 + 40$ seconds). Further growth of the new crack formation.

To give a further impression of the dimensions of the headcut block erosion phenomenon, Figure 4.14 shows a snapshot sequence of the Olympus front view camera recordings during experiment RC3.



4.4 Observations of Experiment RC3

Some very interesting phenomena were observed during experiment RC3. In terms of mass migration rate, massive headcut block erosion is the dominant erosion mechanism and not the continuously headcut undermining erosion process. Headcut undermining takes place on a larger time scale than the headcut block erosion phenomenon.

By freezing the GoPro recording and measuring the yellow-plus grid, it was possible to get a first rough estimation of the headcut migration rate. The horizontal distance was measured at half the headcut height (20 cm) and between the moment of when the crack starts to grow and the moment when the failure block completely detaches from the headcut. Using this method, the headcut migration rate can be as high as **8 cm/s** during the massive block erosion event. While outside these events the migration rate continues continuously with only a few millimeters per second.

Surprisingly, the headcut block erosion mechanism was initiated by a crack near the headcut which was already present. The GoPro snapshots show that the crack widens and penetrates deeper in the clay layer. This may be the result of the positive feedback of three simultaneously acting phenomena which will be discussed further in Chapter 5.

The widening and penetration of the crack takes a few minutes during experiment RC3 due to the resistance (cohesive strength) of the clay package. This resistance may increase if vegetation is present. After the crack reaches the bottom, it can be seen that the eroded block moves horizontally downstream. This process takes a few seconds. After the eroded block has moved a certain distance, it becomes dry because the overflow jet falls in the widening space between the newly formed headcut and the shifted eroded block. Then the block falls forward

downstream due to its own weight and the force of the flowing water, which pushes behind the eroded block.

The tailwater level at the headcut rises until enough hydrostatic pressure has built up to wash away the block residue. Subsequently, the tailwater level drops and the formation of a non-aerated nappe ensures that the continuous headcut undermining process is resumed. If a surface crack is present near the headcut, the block erosion process repeats itself, starting from the next crack. In addition, headcut undermining occurs continuously.

Similar observations were obtained from RC4-6. In these experiments the influence of cracks was significant on both the mass surface erosion and headcut block erosion process. This confirms and underlines the first order assumption that if cracks are present in the surface layer, block erosion is not induced by headcut undermining at the bottom, but starts from mass surface erosion and crack development in the top layer. Unfortunately, large pieces of adhering clay obstructed visibility and water flow during the experiments, limiting successful observational analysis.

4.5 Results of Experiment TP2

This section shows the results of experiment TP2, with concrete plywood panels covering the top of the clay package until the headcut. At the start of this experiment, the river clay headcut had migrated past halfway window 3, in front of GoPro 3 (see Figure 2.1). This is due to erosion during the previous experiments.

After the desired hydraulic conditions were reached, these were kept constant afterwards. Figure 4.15 - Figure 4.19 show snapshots of recordings taken by GoPro 3. The first two snapshots provide a visual indication of setting the desired hydraulic conditions, see also the first 250 seconds of Figure 3.9.

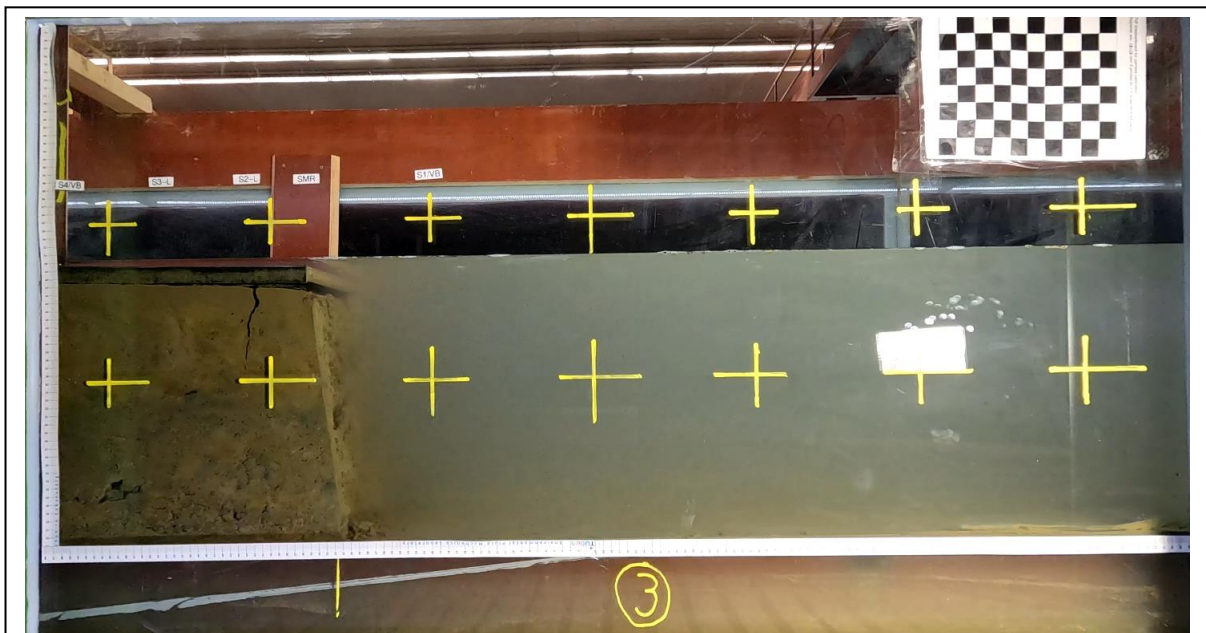


Figure 4.15: Snapshot of GoPro 3 recordings at the start of experiment TP2 ($t=t_0$).

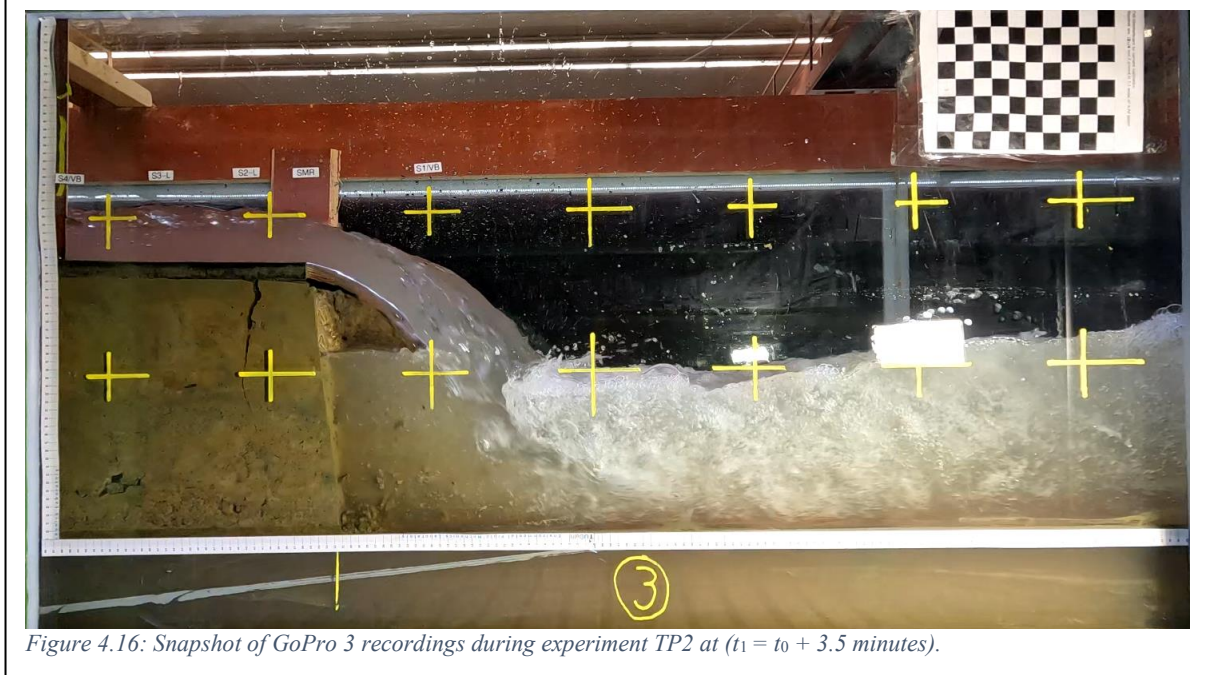


Figure 4.16: Snapshot of GoPro 3 recordings during experiment TP2 at ($t_1 = t_0 + 3.5$ minutes).

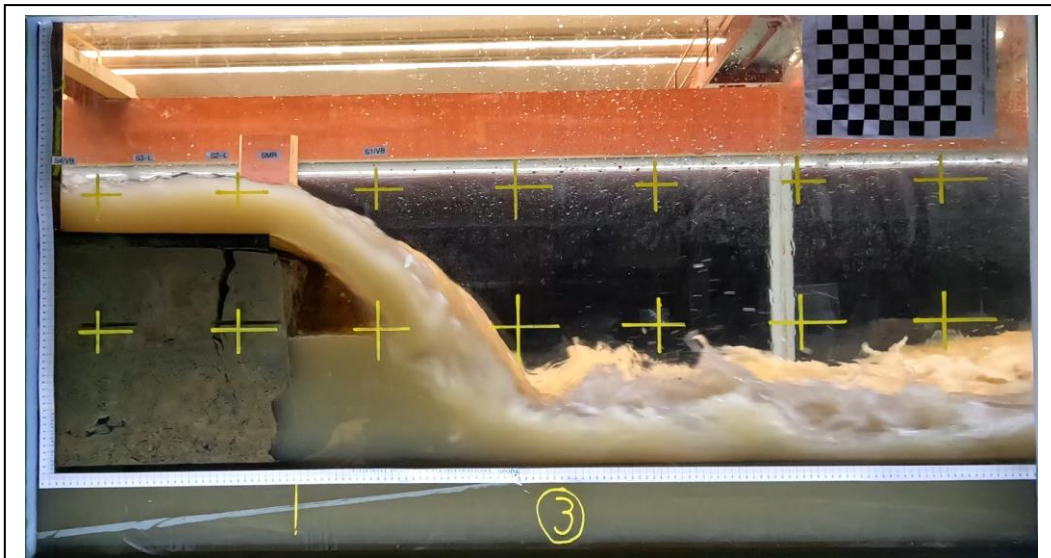


Figure 4.17: Snapshot of GoPro 3 recordings during experiment TP2 at ($t_2 = t_0 + 43$ minutes).

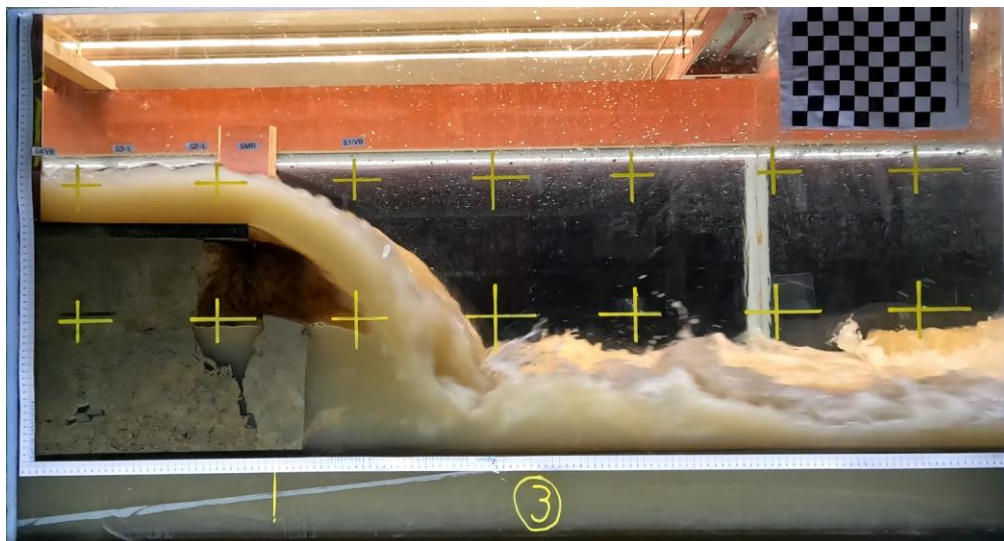


Figure 4.18: Snapshot of GoPro 3 recordings during experiment TP2 at ($t_3 = t_0 + 45$ minutes).

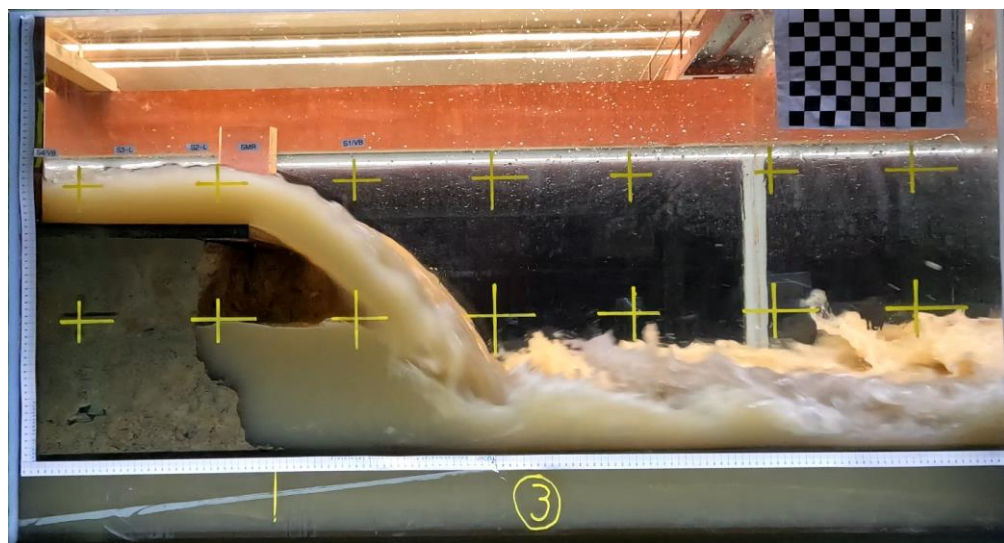


Figure 4.19: Snapshot of GoPro 3 recordings during experiment TP2 at ($t_4 = t_0 + 55$ minutes).

4.6 Observations of Experiment TP2

A crack had already been identified before the start of the experiment and is clearly visible in the first GoPro snapshot, see Figure 4.15. The headcut undermining process could be clearly observed from the start of the experiment. We see that the submerged part of the headcut is continuously eroded grain by grain, making it a slow process. The identified crack starts to grow and consequently headcut block erosion is initiated. This may be due to the undermining process or due to the additional forces arising from the aerated nappe dynamics, which will be discussed further in Chapter 5. The distance from the crack until the headcut was approximately 10 cm. The failure block did not contain the full sediment flume width as water was observed in the crack. After 43 minutes, the failure block begins to slide and rotate while the crack has only penetrated half of the clay package. Unfortunately, we see that because the clay failure block sticks to the glass wall, the headcut block erosion process is slowed down. When the failure block has been washed away, the headcut had migrated too far from the edge of the top cover panel for eddies to have a significant erosion effect (Patil, Mudiyansele, Bricker, Uijtewaal, & Keetels, 2018). Only one headcut block erosion event was observed during experiment TP2.

Also for this experiment, a rough estimate of the headcut migration rate can be obtained from the snapshots, using the same method as for experiment RC3. In this case, during the headcut block erosion event, a migration rate as low as **0.2 cm/s** was found. In addition, headcut undermining occurred continuously which resulted in a migration rate of a few millimeters per second.

Even though a measure was taken to prevent headcut block erosion, this was nevertheless observed during experiment TP2. This time, however, caused by a different mechanism than was the case without the top-layer cover (experiment RC3).

No headcut block erosion was observed during experiment TP1. Only headcut erosion due to a continuously undermining of the submerged part of the headcut caused a regression of only a few centimeters in 44 minutes.

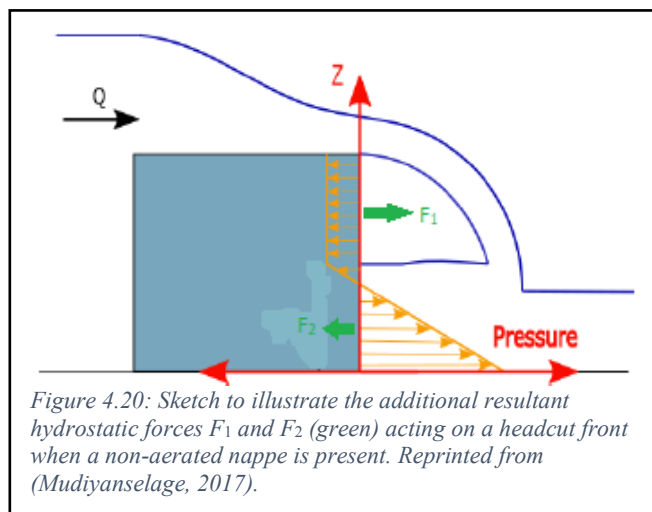
Crack growth was also observed during experiment TP3, but only after an aerated nappe was created several times manually using a tube. The crack grew very slowly as the failure block was obstructed by the top panel at the headcut. Block erosion was initiated by manually pulling up the panel. The headcut had then migrated too far below the panel, so that the vortices could no longer reach the headcut and erosion was no longer observed.

4.7 Improving the Extended BRES Model

As shown in the previous sections, the headcut block erosion mechanism was initiated by a crack near the headcut which was already present. During the erosion process the observed crack widens and penetrates deeper in the clay layer. This may be the result of the positive feedback of three simultaneously acting phenomena:

1. The presence of mass erosion widens the crack. When substituting the conditions of experiment RC3: with the measured crest flow velocity, $U_c = 0.94$ m/s, mass density $\rho = 1000$ kg/m³ and undrained shear strength, $c_u = 36.0$ kPa (see Table 3.2), into the mass erosion criterion of (Winterwerp, Van Kessel, Van Maren, & Van Prooijen, 2021), equation (1.1), we see that the criterion is fulfilled. The criterion shows that the kinetic energy induced by the hydraulic conditions dominates the undrained shear strength, a geotechnical property of the soil.
2. As the crack widens and penetrates deeper into the soil layer, the hydrostatic pressure in the crack water column behind the failure block increases. The additional increasing resultant hydrostatic force pushes against the failure block.

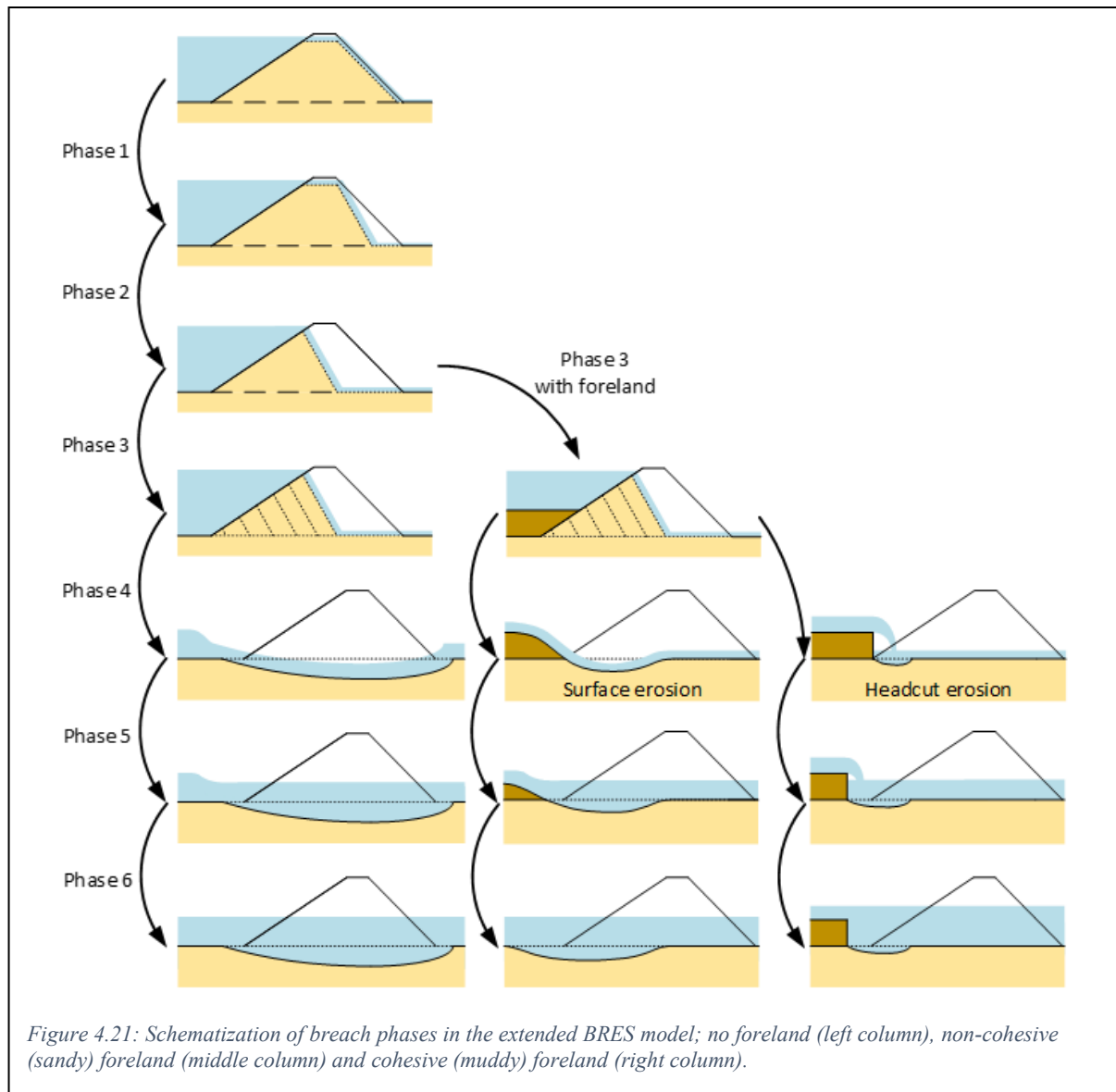
3. The stability of the failure block is influenced by the hydrodynamics of the nappe dynamics. Figure 4.20 shows the horizontal pressure gradient and resultant hydrostatic horizontal forces, F_1 and F_2 , acting on the headcut front during the observed non-aerated (depressed) nappe. The sub-atmospheric pressure under the non-aerated nappe results in a 15-



30% additional horizontal force (F_1) pulling on the failure block (Patil, Mudiyanselage, Bricker, Uijttewaal, & Keetels, 2018). Additionally, the presence of air bubbles in the water column near the headcut, coming from the diverted impinging overflow jet, decreases the local density in the water column. This phenomenon decreases the resultant hydrostatic force (F_2) which pushes against failure block.

These three phenomena should be included in the extended BRES model.

Figure 4.21 illustrates the five breach phases, as they are simulated in the BRES model. The left column indicates the situation without a foreland. The middle column includes a non-cohesive foreland, for instance consisting of sand; the right column presents the implementation of a cohesive foreland (such as clay) in the BRES model. The mass erosion criterion and the three additional forces should be implemented in the extended BRES model in phases 3-6, in the situation where the foreland type consists of cohesive material.



5 Discussion

This chapter includes the discussion of the overall findings and limitations when performing foreland stability experiments in the sediment flume facility.

5.1 Foreland Stability in Reality

Although this study concludes that cracks can have a severe effect on the stability of forelands consisting of river clay, we stay within the constraints of sediment availability and the sediment flume facility. The question remains to what extent our results can be extrapolated to reality: an actual foreland-dike breach. In real life, the stability of forelands depends on aspects such as the sediment composition, geometry, hydraulic conditions, and the presence of vegetation.

Sediment

The river clay tested in this study had specific characteristics. Other types of clay, with different properties, or a specific sand-silt-clay mixture will give different results. Not all clays are equally susceptible to crack formation when the foreland is exposed to a dry period. Clays without cracks, or less cracks, will probably lead to a lower erosion rate. Moreover, clays with a higher cohesivity than the clay used in this study will be more resistant against block erosion. Therefore, it is important to note that the results from the North Sea sand and river clay erosion experiments performed during this study should not be blindly extrapolated to other sediment types.

During the preparation of the sediment package, there were no benthic communities observed. In reality, benthic organisms might strongly influence the soil stability. On the one hand, they will increase the permeability of the soil by making burrows, which makes a foreland vulnerable during high flow velocities (Volkenborn, Polerecky, Hedtkamp, Van Beusekom, & De Beer, 2007). On the other hand, microorganisms will produce and introduce bio-enzymes in the soil. These enzymes are stabilizing the soil by means of chemical reactions.

Geometry and Hydraulic Conditions

The experiments were performed in a setup with dimensions as close to reality as possible. However, dimensions and conditions that occur in an actual breach could not be realized. In the sediment channel a foreland was simulated by means of a sediment package with suitable dimensions. In reality, more extreme hydraulic conditions will prevail, consequently, erosion effects will be more severe.

Headcut erosion will also take place in 3D, this third dimension is likely to ensure that the foreland is actually stronger due to the creation of back pressure.

In reality, the headcut height will be much larger (several meters). Also, the foundation composition – wooden panels in the experiments – will be different. These will affect local flow conditions and thereby erosion mechanisms.

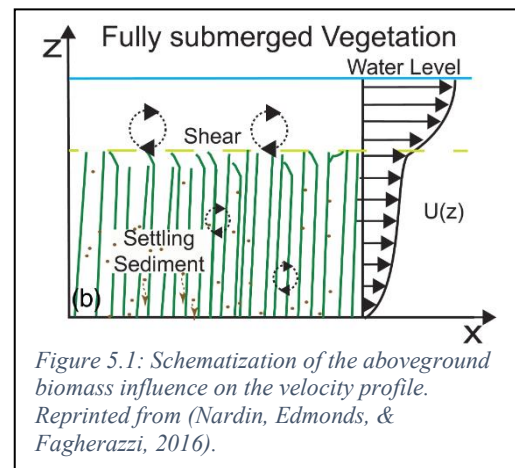
During the river clay experiments it was observed that mass surface erosion flattens the vertical headcut. In reality, the headcut will probably maintain its vertical position because the undermining process is amplified and will therefore have more impact on the headcut foot.

The influence of vegetation

A salt marsh influences the stability of the foreland by defending it against the extreme hydrodynamic forces that occur during a breach (Brooks, et al., 2020; Nardin, Edmonds, & Fagherazzi, 2016; Schoutens, et al., 2022). Considering stratigraphy, salt marshes can be seen as two layers: the surface and the root system (aboveground and belowground biomass).

Surface: the aboveground biomass (stems) influences the high flow velocity profile (Klok, 1996). The bed shear stress and surface erosion are reduced. Nevertheless, scour can occur due to turbulence and vegetation scarcity (see Figure 5.1).

Root system: fibrous materials provide tensile strength. If the belowground biomass increases, the tensile strength increases and therefore the headcut erosion is restricted.



It is still unclear what the quantitative effect of cracks is on the stability of a vegetated foreland when it is subject to (sudden) high-water events. Roots of vegetation can act as a kind of reinforced concrete, thereby reducing the weakening by cracks.

5.2 The Use of a Broad-Crested Weir as Experimental Setup

A broad-crested weir, installed in a sediment flume facility, provides an opportunity to conduct foreland erosion experiments. However, during each North-Sea sand experiment, a scour hole developed upstream: the sudden change of bottom friction due to a change in material type over the broad crested weir had influenced the experiments. Another construction is needed to prevent this artefact. The falling gate construction is a useful adjustment for setting the desired initial water level difference between the upstream and downstream section of the flume.

With respect to the sensors, embedding the magnet of a magnetostrictive position sensor in Styrofoam allows for stable measurements even during chaotic flow conditions. Care should be taken that the EMS-probe is fully immersed in the water column. Gopros tend to become warm after some 30 minutes, cooling should be provided for longer measurements. During the clay experiments, the clay sticks to the plexiglass walls, which made some erosion phenomena difficult to observe.

Proper attention is required to prepare the soil package in the right condition: stones need to be removed; moistening followed by drying is needed to make it homogeneous. The circulating water became more and more turbid due to the eroded sediment. For optimal experiments, where constant erosion conditions are important, the water should be filtered, and the flume should be cleaned after each test.

An unwanted peak occurred in the shear strength curve during the shear box tests performed with the river clay samples. The peak was caused by very small rocks in the sample that resisted shearing.

Covering the sediment with plywood panels - referred to as the Tompouce setup – is a promising and enriching innovation of the facility, which enables studying clay erosion with a focus on headcut undermining instead of headcut block erosion. A limitation of this setup, however, is that after a block erosion event, occurring under the installed panels, the headcut front is too far for the eddies to have a significant erosion effect.

Since the surface of the sediment test layer was not in all cases completely horizontal – especially with the Tompouce experiments – a critical flow could not be maintained over the full crest length. A hydraulic jump occurred in these situations, which influenced the nappe formation and thereby the erosion process.

6 Conclusions

As an objective for this study, the following main research question has been formulated:

“Which erosion mechanisms are important to consider for forelands under dike breach conditions?”

The answer will be provided based on three sub-questions.

- Sub-question 1: Which erosion mechanisms can be observed under dike breach conditions?”

Dike breach conditions were approximated successfully in the experimental setup. The broad-crested weir construction provided high critical flow over the surface of the sediment package, mimicking a foreland. Three erosion mechanisms were observed: surface erosion, headcut erosion due to undermining and headcut block erosion, due to the formation of cracks in the surface layer. The latter process turned out to be a new mechanism, which was not foreseen and became an important outcome of this work.

- Sub-question 2: Which of these mechanisms are most dominant for sand and which one for clay during breach conditions?”

Surface erosion dominates the erosion of **sandy** forelands, with a fast erosion process as a result. A headcut does not develop.

For forelands consisting of **clay**, headcut erosion due to undermining is a continuous process by eddies due to overflow jet impingement. However, for the river clay analyzed in this study, where cracks were abundantly present, massive block erosion is the dominant erosion process, dominant in terms of mass and migration rate.

The headcut block erosion mechanism occurs intermittently. Here, vulnerable cracks, already present near the headcut, grow due to high flow velocities and additional horizontal forces. These cracks widen and penetrate deeper in the soil layer; the block shifts downstream. Thereafter, the block rotates and falls forward. A non-aerated nappe occurs after the block residue is washed away and the downstream water level has decreased. The block erosion process repeats itself, starting from the next crack.

Interestingly enough, block erosion is not primarily induced by headcut erosion at the bottom, but starts from mass-erosion and crack development in the top layer.

- Sub-question 3: Which foreland sediment type: sandy, muddy or vegetated is most suitable to reduce flood risk?

As expected, a **sandy** foreland without vegetation was easily eroded by surface erosion during the experiments. The mean migration rate, the retreat of the headcut front, measured was approximately 3 cm/s. In our case, maximum flow velocities of 2 m/s were obtained. During a real breach situation, however, flow velocities as high as 10 m/s can be reached. Due to the phenomenon of dilatancy, the pick-up flux can be lower at these high velocities (Alhaddad, 2021) (Bisschop, Miedema, Visser, Keetels, & Van Rhee, 2016). This phenomenon will probably increase the stability of the foreland. Still, the overall effectiveness of a sandy foreland to mitigate breach development is considered to be very minimal to negligible.

A foreland consisting of **river clay** is far more stable. The erosion process proceeds in a much slower timespan under dike breach conditions. Without cracks, the migration rate can be as low as a few centimeters per hour. However, if cracks are present in the clay layer, stability is worsened considerably, leading to intermittent migration rates as high as 8 cm/s.

As discussed in Section 5.1, **vegetation** (salt marsh) growth on a foreland is expected to provide an extra positive dimension to its stability, hence reducing flood risk even more. The temperate flow velocity profile near the bed, caused by the stems, is favorable for reducing surface erosion. The increase of the tensile strength of the soil due to the belowground biomass will resist headcut erosion. But also here, cracks will have a negative effect on stability.

Finally, this enables us to answer the main research question, “*Which erosion mechanisms are important to consider for forelands under dike breach conditions?*”. For non-cohesive sediments, surface erosion should be considered as the dominant erosion mechanism. In case of cohesive sediments, however, headcut block erosion should be considered as the dominant erosion mechanism. Here, when cracks are present, the erosion rate increases considerably. Especially the latter effect is a new finding; this mechanism should be included in foreland-dike breach development modelling.

The data obtained in this experimental study can serve well for validation purposes of both physical and numerical models.

7 Recommendations

After having found the dominant foreland erosion mechanisms, some suggestions for future studies on the intriguing topic of foreland stability under dike breach conditions can be formulated.

- Advanced methods of fully automatic tracking of the headcut outline using numerical methods from camera images (i.e., Canny Edge Detection) should be explored, even in turbid water conditions (see Chapter 4.1). As a result, more accurate predictions can be made of the headcut migration rate and thus the behavior and stability of the foreland.
- The experiments with the maintained conditions in the sediment flume facility should be continued with more developed foreland sediment packages, such as fully grown salt marshes. A comparison with this study can be made by focusing on how the vegetation influences the stability of a foreland with surface cracks during dike breach conditions. The vegetation will probably reinforce the soil layer and thereby influence the headcut block erosion process. A next step could be to study different types of vegetation with different characteristics (strength of the stem, leaf area, root density etc.), which will most likely offer different outcomes.
- This study was limited to a 2D-perspective. In reality, 3D-effects will be present. These effects should be studied in large scale setups or physical models. This requires a much wider setup. Consequently, outdoor measurements could be of interest here. In order to record the effects in the 3rd dimension in the desired detail in these types of conditions, suitable measurement techniques must be considered.
- The broad-crested weir had a solid, non-erodible false bottom. It is interesting to investigate foreland erosion in a setup that mimics reality better, i.e. with an erodible bottom (Stein, Julien, & Alonso, 1993). This can be done by filling the cavity of the false bottom – below the sediment – with the desired sediment mixture. Alternatively, outdoor measurements in the field where an erodible soil is already present may be a possibility.

- The effects of climate change, such as sea-level rise and long periods of drought, may increase or decrease the formation of cracks in, for instance, salt marshes. Since cracks appear to have a dominant effect on the erosion rate, it is interesting to study the process of crack formation, crack detection and methods for preventing crack formation in the foreland sediment. For dikes, this is already an ongoing study. An example of a promising detection technique was recently done by (De Roos, 2022). Here cracks are detected by means of a fiber optic cable, using distributed temperature sensing. Because forelands are quite dynamic areas where sometimes severe hydraulic conditions prevail, damage to the cables can occur what makes this technique not reliable yet. A suggestion could be to mount optical remote-sensing on drones for visual inspection. This technique is already being used for the inspection and monitoring of civil structures, see for example the publication of (Li & Liu, 2018).
- The influence of surface cracks on headcut block erosion should be incorporated in foreland erosion physical and mathematical numerical models. Such as, for example, the BRES-2021 module. As a first-order approximation, the presence or absence of surface cracks, along with the concentration, can be a parameter. This parameter might influence the soil interaction forces by reducing the soil shear and tensile strength. In addition, the calculation of the width of the failure block for cohesive sediments via the moment balance, and thereby the headcut erosion rate, could perhaps be expanded with the three phenomena as described in section 4.7. Three additional horizontal forces occur because of crack penetration and the hydraulic conditions at the headcut. To add these forces in the momentum balance, the pore pressure at the surface crack location, the density of the tailwater and the pressure in the nappe cavity, among others, must be measured accurately. As has been done, for example, by (Mudiyanselage, 2017) and (Alhaddad, 2021).
- Since Nature-based Solutions generally require less maintenance and can often help to reduce long-term costs, would it be interesting to study the cost-effectiveness of a foreland in comparison with a more traditional alternative in more detail. A possible method could be via a Cost-Benefit Analysis, see also (De Vries, Van Koningsveld, Aarninkhof, & De Vriend, 2021).

References

- Abdalla, M. G., & Shamaa, M. T. (2016, January-February). Experimental Investigations of Nappe Profile and Pool Depth for Broad. *International Journal of Engineering Research and General Science*, pp. 593-610. Retrieved from www.ijergs.org
- Alhaddad, S. M. (2021). *Breaching Flow Slides and the Associated Turbidity Currents: Large-Scale Experiments and 3D Numerical Modelling*. Delft: TU Delft. Retrieved from <https://doi.org/10.4233/uuid:f41b33db-30ce-42d5-9cad-06d12c50d90f>
- Badr, K., & Mowla, D. (2014, December 1). Development of Rectangular Broad-crested Weirs for Flow Characteristics and Discharge Measurement. *KSCE Journal of Civil Engineering*, 2015, pp. 136-141. doi:10.1007/s12205-012-0433-z
- Bensoula, M., Missoum, H., & Bendani, K. (2014, December). Critical undrained shear strength of sand-silt mixtures under monotonic loading. *Earth Sciences Research Journal*, pp. 149-156.
- Bisschop, F., Miedema, S. A., Visser, P. J., Keetels, G. H., & Van Rhee, C. (2016). Experiments on the Pickup Flux of Sand at High Flow Velocities. *J. Hydraul. Eng.*, pp. 1-11. doi:10.1061/(ASCE)HY.1943-7900.0001142
- Brooks, H., Möller, I., Carr, S., Chirol, C., Christie, E., Evans, B., . . . Royse, K. (2020, June 9). Resistance of salt marsh substrates to near-instantaneous hydrodynamic forcing. *EARTH SURFACE PROCESSES AND LANDFORMS*, 2021, pp. 67-88. doi:10.1002/esp.4912
- Chanson, H., & Eraso, V. (2004). Design of weirs and spillways., (pp. 391-430). Retrieved from https://www.academia.edu/8814428/Design_of_weirs_and_spillways
- Cheng, C. H., De Smit, J. C., Fivash, G. S., Hulscher, S. J., Borsje, B. W., & Soetaert, K. (2021, March 2). Sediment shell-content diminishes current-driven sand ripple development and migration. *Earth Surface Dynamics Discussions*, pp. 1-26. doi:<https://doi.org/10.5194/esurf-2021-13>
- De Roos, S. (2022). *Crack detection for dikes using distributed temperature sensing*. MSc Thesis, Delft University of Technology, Delft.
- De Vries, M., Van Koningsveld, M., Aarninkhof, S. G., & De Vriend, H. (2021). A systematic design approach for objectifying Building with Nature solutions. *Research in Urbanism Series*, pp. 29-50. doi:<https://doi.org/10.47982/rius.7.124>

- Deltares. (2022). Instrument, Programmable electromagnetic liquid velocity meter. (Version 1.1). Delft, The Netherlands. Retrieved from <https://www.deltares.nl/app/uploads/2016/04/Programmable-electromagnetic-liquid-velocity-meter.pdf>
- Endress+Hauser. (2011, August). Technical Information Proline Prosonic Flow 91W: Ultrasonic Flow Measuring System Flowrate measurement for standard applications with drinking water and process water. Instruments International AG; Kaegenstrasse 2, 4153 Reinach, Switzerland.
- Engelund, F., & Hansen, E. (1967). *a monograph on sediment transport in alluvial streamns*. Copenhagen: Technical University of Denmark.
- Gerritsen, H. (2005). What happened in 1953? The Big Flood in the Netherlands in retrospect. *Philos. Trans. R. Soc.*, pp. 1271–1291.
- Isbash, S. (1932). *CONSTRUCTION OF DAMS BY DUMPING STONES INTO FLOWING WATER*. United States Engineer Office, Engineering Division. Leningrad: War Department.
- Kim, I. C., & Suh, K. D. (2018, July 19). Effect of Sea Level Rise and Offshore Wave Height Change on Nearshore Waves and Coastal Structures. *Journal of Marine Science and Application*, pp. 192-207. doi:<https://doi.org/10.1007/s11804-018-0022-8>
- Klok, P. (1996). *De verborgen kracht van riet. De invloed van de beweging van riet op de golfdempende werking ervan*. Delft: Delft University of Technology.
- Laboyrie, H. P., Van Koningsveld, M., Aarninkhof, S. G., Van Parys, M., Lee, M., Jensen, A., . . . Kolman, R. (2018). *Dredging for sustainable infrastructure*. CEDA/IADC.
- Li, Y., & Liu, C. (2018). Applications of multirotor drone technologies in construction management. *International Journal of Construction Management*. doi:10.1080/15623599.2018.1452101
- Lohithaswa, M. H. (2015, Jan-Feb). Canny Edge Detection Algorithm on FPGA. *IOSR Journal of Electronics and Communication Engineering (IOSR-JECE)*, pp. 15-19. doi:10.9790/2834-10111519
- Marijnissen, R., Kok, M., Kroeze, C., & Van Loon-Steensma, J. (2020, January 15). The Sensitivity of a Dike-Marsh System to Sea-Level: A Model-Based Exploration. *Marine Science and Engineering*, 2020(42), pp. 1-17. doi:10.3390/jmse8010042
- Masson-Delmotte, V., Zhai, P., & WG1. (2021). *Climate Change 2021: The Physical Science Basis, Summary for Policymakers*. Switzerland: Intergovernmental Panel on Climate Change.

- Microsonic GmbH. (2022, 09 26). Extract from our online catalogue: mic+35/IU/TC. 44263 Dortmund, Germany.
- Mudiyanselage, S. D. (2017). *Effect of Nappe Non-aeration on Caisson Sliding Force during Tsunami Breakwater Overtopping*. Delft. Retrieved from <http://repository.tudelft.nl/>
- Nardin, W., Edmonds, D. A., & Fagherazzi, S. (2016, January 9). Influence of vegetation on spatial patterns of sediment deposition in deltaic islands during flood. *Advances in Water Resources*, pp. 236-248. Retrieved from : www.elsevier.com/locate/advwatres
- Osman Akan, A., & Iyer, S. (2021). Hydraulic Structures. In A. Osman Akan, & S. Iyer, *Open Channel Hydraulics* (Second Edition ed., pp. 213-304). Elsevier Inc. doi:<https://doi.org/10.1016/C2019-0-03618-7>
- Partheniades, E. (1962). *A study of erosion and deposition of cohesive soils in salt water*. Berkeley, USA: University of California.
- Patil, A., Mudiyanselage, S., Bricker, J., Uijttewaal, W., & Keetels, G. (2018). Effect of overflow nappe non-aeration on tsunami breakwater failure. *Proceedings of the Coastal Engineering Conference, 36*, (p. 18). doi:10.9753/icce.v36.papers.18
- Robinson, M., & Hansen, G. (1994). A Deterministic Headcut Advance Model. *Transactions of the ASAE Vol.37(5)*, pp. 1437-1443.
- Schiereck, G., & Visser, P. (2021, juni). De Sint-Elisabethsvloed en de onafwendbare teloorgang van de Grote Waard. *Tijdschrift voor Waterstaatsgeschiedenis*, 30, pp. 13-25.
- Schoutens, K., Stoorvogel, M., Van den Berg, M., Van den Hoven, K., Bouma, T. J., Aarninkhof, S. G., . . . Temmerman, S. (2022, July). Stability of a Tidal Marsh Under Very High Flow Velocities and Implications for Nature-Based Flood Defense. *Frontiers in Marine Science*. doi:10.3389/fmars.2022.920480
- Shields, A. (1936). *APPLICATION OF SIMILARITY PRINCIPLES AND TURBULENCE RESEARCH TO BED-LOAD MOVEMENT*. Hydrodynamics Laboratory, Soil Conservation Service. Berlin: California Institute of Technology.
- Smid, J. (2021). *The effects of forelands on embankment breaching in coastal and river regions*. MSc Thesis for Delft University of Technology, TU Delft, Delft.
- Stein, O. R., Julien, P. Y., & Alonso, C. V. (1993). Mechanics of jet scour downstream of a headcut. *Journal of Hydraulic Research*, pp. 723-737.
- TAW. (1998). *Grondslagen voor waterkeren*. Rijkswaterstaat. TAW. Retrieved from https://puc.overheid.nl/doc/PUC_27996_31

- Temmerman, S., Meire, P., Bouma, T. J., Herman, P. M., Ysebaert, T., & De Vriend, H. J. (2013, December 5). Ecosystem-based coastal defence in the face of global change. *Nature*(Vol 504), pp. 79-83. doi:0.1038/nature12859
- Temposonics GmbH & Co. KG. (2015, September). Data Sheet: G-Series GP/GH Analog/Digital Outputs, Magnetostrictive Linear Position Sensors. (Revision G). 58513 Lüdenscheid, Germany. Retrieved from <http://www.temposonics.com>
- Uijtewaal, W. (2022). Lecture Notes: Turbulence in Hydraulics, CIE5312. Delft Technical University.
- Van Gerven, K. A. (2004). *Dijkdoorbraken ontstaan, voorkomen en bestrijden*. Utrecht: STOWA.
- Van Rijn, L. C. (1984). Sediment Transport, Part I, II & III. *J. Hydr. Eng.*, pp. 1431-1641.
- Verwaal, W., & Mulder, A. (2017). *Soil mechanics laboratory manual*. Delft: Delft Technical University.
- Visser, P. J. (1988). A model for breach growth in sand-dikes. *Proc. 21st Int. Conf. Coastal Eng.*, (pp. 1897-1910). Malaga, Spain. doi:DOI: 10.9753/icce.v21.140
- Visser, P. J. (1995). *APPLICATION OF SEDIMENT TRANSPORT FORMULAE TO SAND-DIKE BREACH EROSION*. Faculty of Civil Engineering, Delft University of Technology, Hydraulic and Geotechnical Engineering Division. Delft: Communicastions on Hydraulic and Geotechnical engineering.
- Visser, P. J. (1998). *Breach growth in sand-dikes*. Delft: Delft University of Technology.
- Volkenborn, N., Polerecky, L., Hedtkamp, S. I., Van Beusekom, J. E., & De Beer, D. (2007). Bioturbation and bioirrigation extend the open exchange regions in permeable sediments. *Limnology Oceanography*, 2007, pp. 1898-1909. Retrieved from <https://aslopubs.onlinelibrary.wiley.com/doi/10.4319/lo.2007.52.5.1898>
- Vrijling, J. K., Schweckendiek, T., & Kanning, W. (2011). *Safety Standards of Flood Defenses*. Delft. Retrieved from <https://www.researchgate.net/publication/254908290>
- Vuik, V., & Jonkman, S. N. (2018, December). How vegetated foreshores affect probabilities and consequences of dike failure. *Coastal Engineering Proceedings*, pp. 1-2. doi:10.9753/icce.v36.risk.61
- Vuik, V., Jonkman, S. N., Borsje, B. W., & Suzuki, T. (2016, juni 15). Nature-based flood protection: The efficiency of vegetated foreshores for reducing wave loads on coastal dikes. *Coastal Engineering*(116), pp. 42-56.

- Wilson, K. C., & Nnandi, F. N. (1992). Mobile bed-friction at high shear stress. *J. Hydr. Eng.*(vol. 115), pp. 2917-2925.
- Winterwerp, J. C., Van Kessel, T., Van Maren, D. S., & Van Prooijen, B. C. (2021). Erosion of cohesive sediment - pick-up functions for non-equilibrium conditions. In *Fine Sediment in Open Water: From Fundamentals to Modeling* (pp. 179-221). London: World Scientific.
- Zhu, Y. H., Visser, P. J., & Vrijling, J. K. (2006). A model for headcut erosion during embankment breaching. *River, Coastal and Estuarine Morphodynamics: RCEM 2005*, pp. 1183-1190.
- Zhu, Y., Visser, P. J., Vrijling, J. K., & Wang, G. (2011, January). Experimental investigation on breaching of embankments. *Science China Technological Sciences*(Vol. 54), pp. 148-155. doi:10.1007/s11431-010-4208-9
- Zhu, Z., Vuik, V., Visser, P. J., Soens, T., Van Wesenbeeck, B., Van de Koppel, J., . . . Bouma, T. J. (2020, October). Historic storms and the hidden value of coastal wetlands for nature-based flood defence. *Nature Sustainability*, pp. 853-862. doi:<https://doi.org/10.1038/s41893-020-0556-z>

Appendix A: Additional Images

Additional images are provided in support of this thesis.



Depressed (non-aerated) nappe during experimental setup test run.



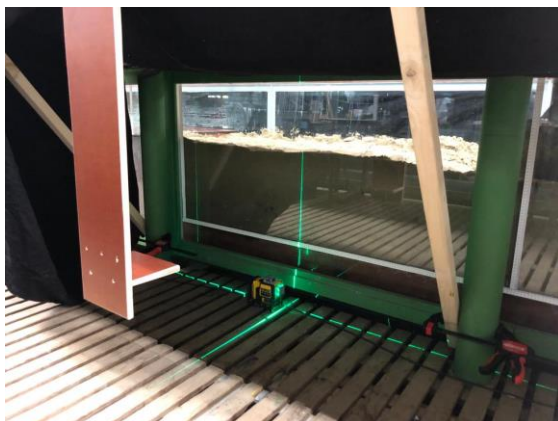
Aerating of the depressed nappe cavity through the aeration tube during the experimental setup test run.



Work space and GoPro setup.



Development of the GoPro setup.



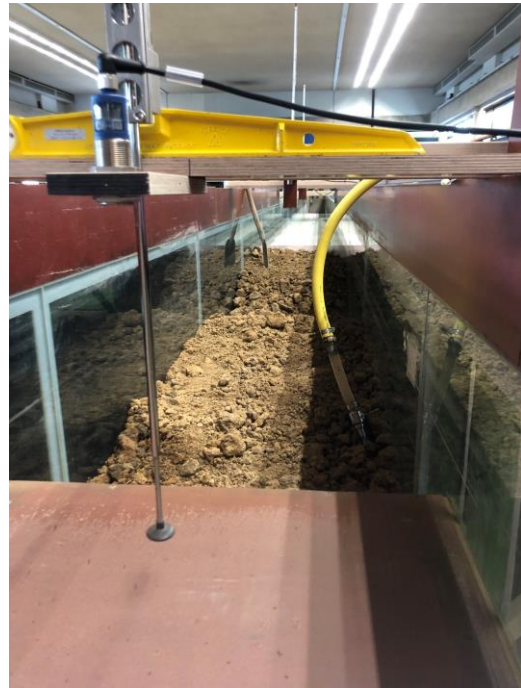
When drawing the yellow plus-grid, a stabilized laser device was used.



Installation and mounting of the ultrasonic echo sensor (type MIC+35).



Installation of the MPS 1 upstream of the broad-crested weir.



Installation of the MIC 1 and EMS on top of the broad-crested weir.



River clay sample containers for the sediment analysis. The containers were stored in a cooled climate room.



Falling gate and vertical lock construction.



Scour hole development at the broad-crested weir during a North Sea sand experiment.



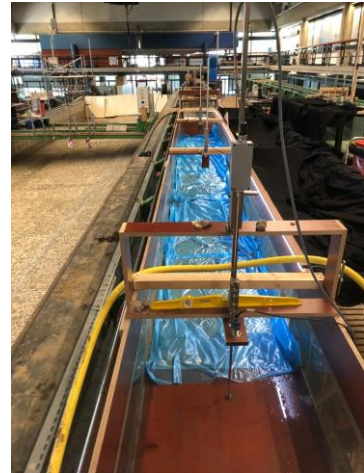
Close-up of the scour hole development at the broad-crested weir material transition during a North Sea sand experiment.



Preparation of the river clay package and installation of MIC 3.



Position and installation of the EMS, MIC 1-3, and preparation of the river clay package.



Large plastic bags were placed over the river clay pack while the pack dried.



Final condition of the river clay package before the start of the experiments.



River clay headcut after removing of the Tompouce setup. The surface cracks are clearly visible.

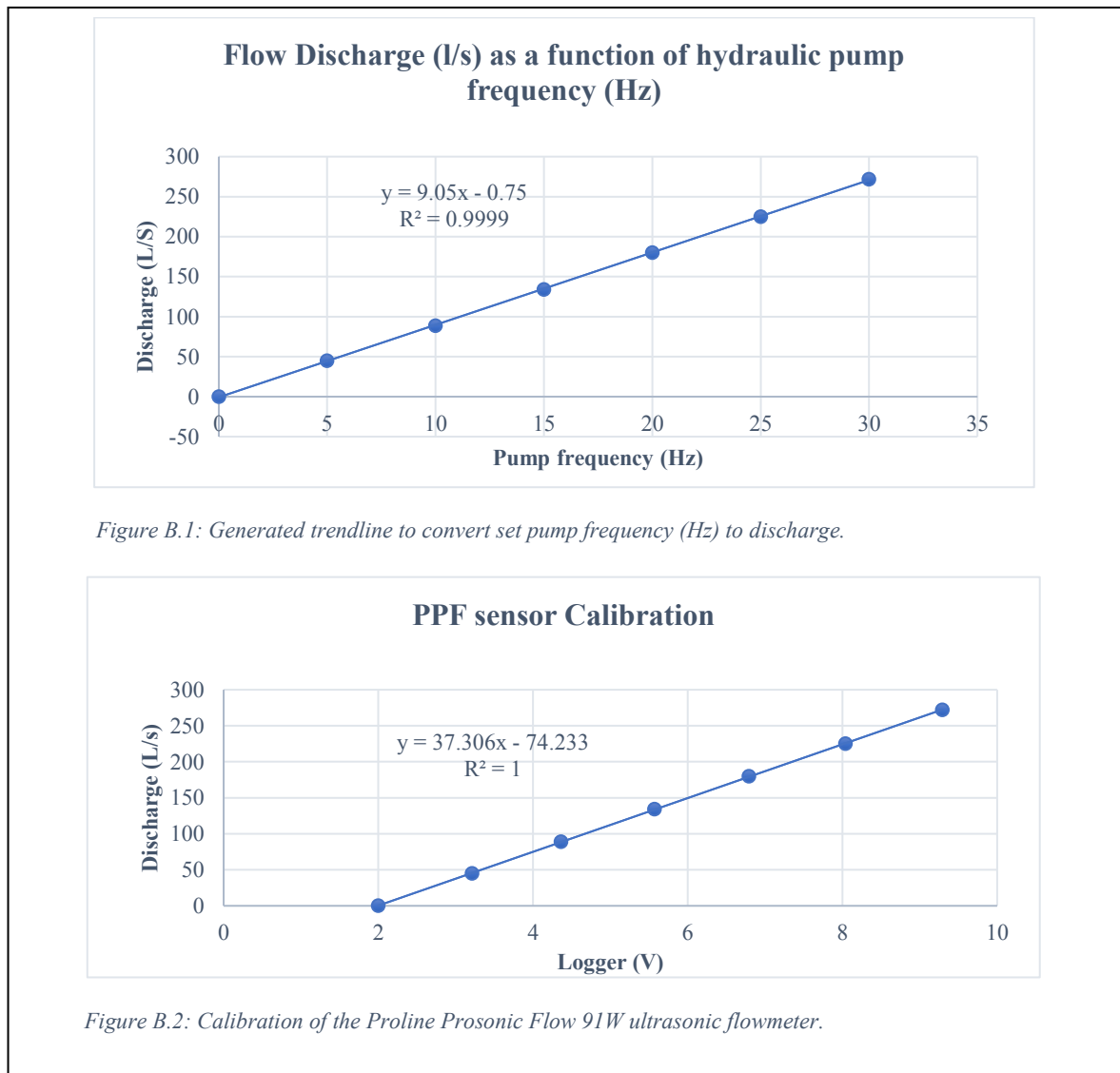
Appendix B: Instruments

This appendix presents the specification tables and generated calibration graphs of the hydraulic measurement instruments used during this study.

Discharge Sensor (PPF)

Table B.1 Specifications of the discharge sensor.

Measuring method	Transit time difference
Manufacturer	Endress+Hauser
Model type	Proline Prosonic Flow 91W
Output	Analogue 0 - 10 V
Flow velocity detection range	0 – 15 m/s
Measurement error	2 %




Electromagnetic Flow Sensor (EMS)

Table B.2 Specifications of the electromagnetic flowmeter.

Measuring method	Conductive liquid moving through a magnetic field
Manufacturer	Deltares National Instruments
Model, ID	Standard, E662
Probe type	E30
Output	Analogue 0 - 10 V
Detection range	0 - 2.5 m/s, bi-axial, 4-quadrant
Accuracy	1% of measured value

EMS calibration certificate

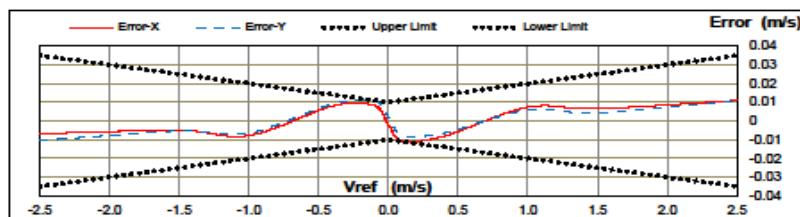
Type: E30
Model: Standard
Identification: E662
S/N: E662
Date: 20 April 2021
Water Temp.: 15.5 °C
Engineer: C. van Nieuwenhuizen
Reviewer: W. Taal
Generic formula's: $|V| = -0.000188 U^2 + 0.1023 |U| + 0.002$ m/s Range: 1.0 m/s
 $|V| = -0.001175 U^2 + 0.2558 |U| + 0.002$ m/s Range: 2.5 m/s
Accuracy: 1% of reading +/- 0.01 m/s
Calibration result: passed



X-direction (PEMS output-0)				Y-direction (PEMS output-1)			
Vref (m/s)	Ux (v)	Vx (m/s)	Error-X (m/s)	Vref (m/s)	Uy (v)	Vy (m/s)	Error-Y (m/s)
-2.501	-10.280	-2.507	-0.007	-2.500	-10.293	-2.511	-0.011
-1.500	-6.044	-1.505	-0.005	-1.500	-6.046	-1.506	-0.005
-1.000	-10.012	-1.007	-0.008	-1.000	-9.999	-1.006	-0.006
-0.400	-3.835	-0.392	0.008	-0.400	-3.823	-0.390	0.009
-0.100	-0.877	-0.092	0.008	-0.100	-0.850	-0.089	0.011
0.000	0.000	-0.002	-0.002	0.000	0.000	0.002	0.002
0.100	0.859	0.090	-0.011	0.100	0.887	0.093	-0.008
0.400	3.839	0.392	-0.008	0.400	3.856	0.394	-0.006
1.000	10.015	1.008	0.007	1.000	9.999	1.006	0.006
1.501	6.053	1.507	0.007	1.501	6.044	1.505	0.004
2.501	10.300	2.512	0.011	2.501	10.298	2.512	0.011

Vref = velocity carriage Calibration Flume
 Uxy = measured output signals PEMS (voltage mode)

Vxy = calculated velocities EMS
 error-XY = Vxy - Vref



Remarks:

Used Equipment:

Signal:	Device:	S/N:	ID-Deltares:	Manufacturer:
output-0 and output-1	PEMS	100198	02.00.368	Deltares
Vref Ux Uy	NI 9205 (An.Inp.Module)	-	-	National Instruments
Complete Case DAQ	cDAQ-9191	-	-	National Instruments

Note:

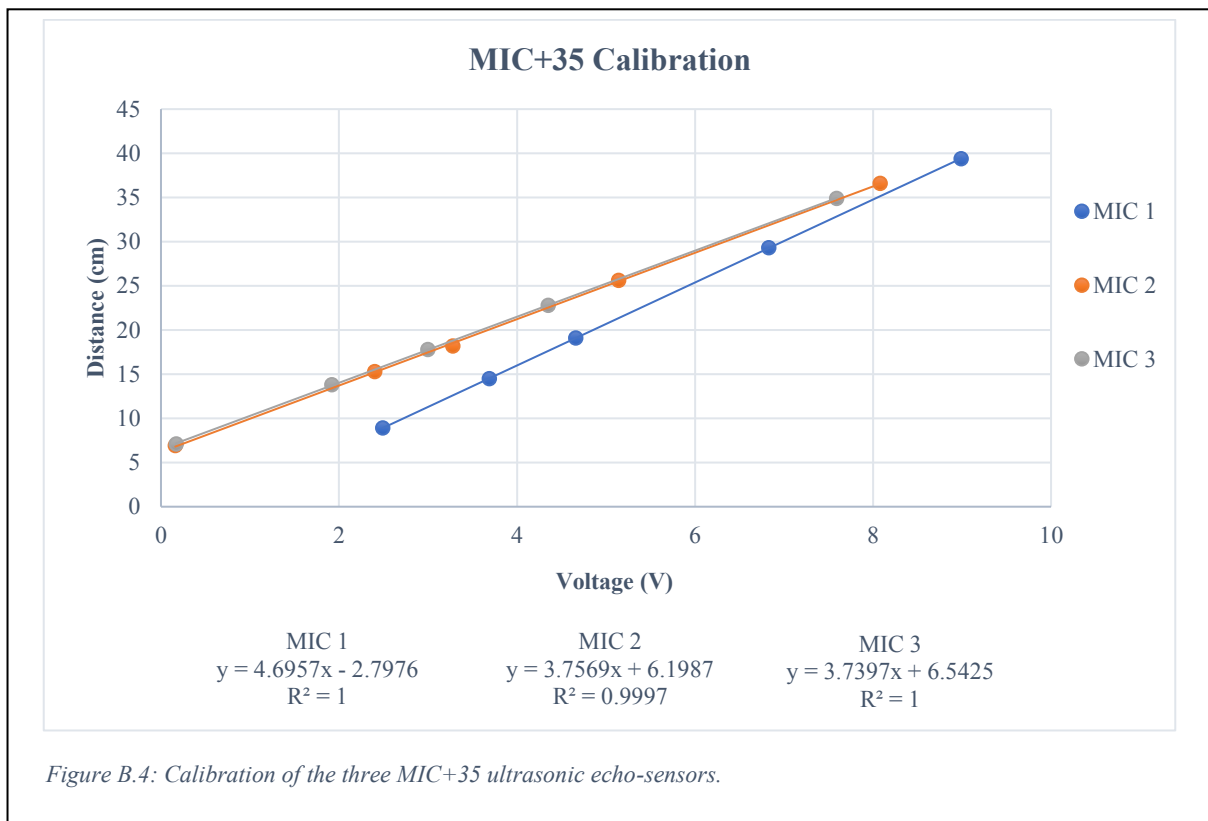
The PEMS can operate in 'voltage' mode or in 'velocity' mode. In 'velocity' mode the Pems software applies the conversion formulae as given above, the results are expressed in m/s. In 'voltage' mode the signals are presented as measured and expressed in volts, the appropriate conversion formula is to be applied then to obtain values in m/s. The PEMS was used in 'voltage' mode during calibration.

Figure B.3: Calibration certificate of the used electromagnetic flowmeter (type E30, E662) provided by Deltares.

Ultrasonic echo-sensors (MIC)

Table B.3 Specifications of the ultrasonic echo-sensor.

Measuring method	Echo propagation time measurement
Manufacturer	Microsonic
Model type	MIC+35
Output	Analogue 0-10 V
Detection range	65-600 mm
Accuracy	± 1% of measured value



Magnetostrictive position sensor (MPS)

Table B.4 Specifications of the magnetostrictive position sensor.

Measuring method	Time-based magnetostrictive position sensing
Manufacturer	Temposonic
Model type	GH rod-style sensor - Magnet float
Output	Analogue -10 to +10 V
Stroke length	1035 mm
Dead zone	63.5 mm
Accuracy	± 0.02 % of measured value

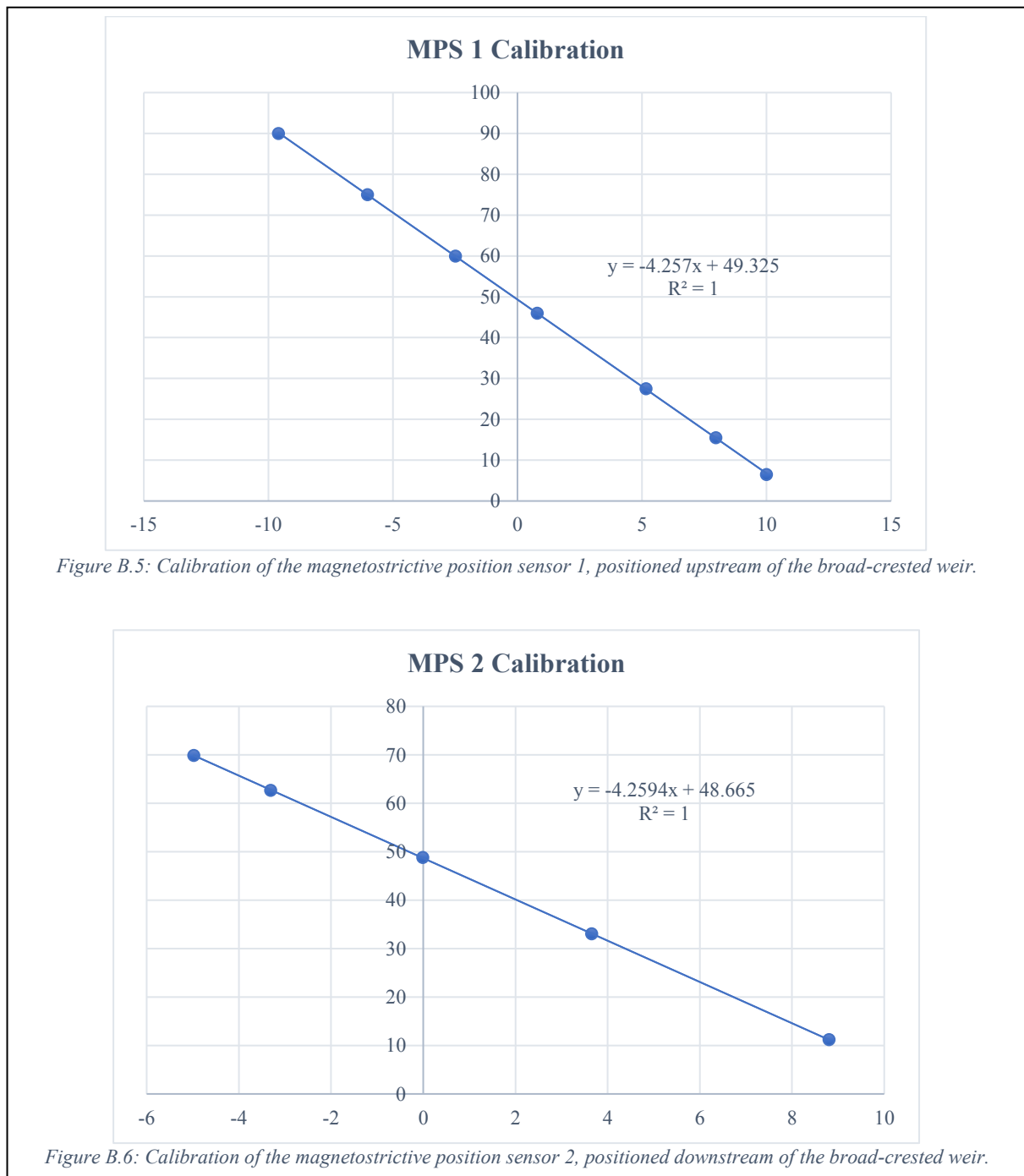


Figure B.5: Calibration of the magnetostrictive position sensor 1, positioned upstream of the broad-crested weir.

Figure B.6: Calibration of the magnetostrictive position sensor 2, positioned downstream of the broad-crested weir.

Appendix C: Available Data

Table C.1 provides the GoPro recording and hydraulic data filenames for each experiment. Because of the maximum file size of 4 Gb (32 bit), a GoPro divides long duration recordings into segments of about 11 minutes, leading to separate data files.

The GoPro recording filename includes the GoPro number (1-5), experimental type, experiment run and GoPro recording part. The hydraulic data filename (DASYlab logs) includes the experimental type and experimental run. *All* data of *all* experiments are available for further analysis on the 4TU.ResearchData Repository.

Table C.1: overview of the available GoPro video recordings and hydraulic data per experiment. The GoPro recording filename includes the GoPro number (1-5), experimental type, experiment run and GoPro recording part. The hydraulic data filename (DASYlab logs) includes the experimental type and experimental run. All data of all experiments are available for further analysis at the 4TU.ResearchData Repository.

	Filename GoPro Video	Filename Hydraulic Data
<u>North Sea sand</u>		
NSS1	<i>GP_1-5_NSSand_01</i>	<i>NSSand_01</i>
NSS2	<i>GP_1-5_NSSand_02</i>	<i>NSSand_02</i>
NSS3	<i>GP_1-5_NSSand_03</i>	<i>NSSand_03</i>
<u>river clay</u>		
RC1	<i>GP_1-5_RClay_01.1-2</i>	<i>RiverClay_01</i>
RC2	<i>GP_1-5_RClay_02.1-3</i>	<i>RiverClay_02</i>
RC3	<i>GP_1-5_RClay_03.1-3</i>	<i>RiverClay_03</i>
RC4	<i>GP_1-5_RClay_04.1-4</i>	<i>RiverClay_04</i>
RC5	<i>GP_1-5_RClay_05.1-6</i>	<i>RiverClay_05</i>
RC6	<i>GP_1-5_RClay_06.1-5</i>	<i>RiverClay_06</i>
<u>Tompouce</u>		
TP1	<i>GP_1-5_Tompouce_01.1-6</i>	<i>Tompouce_01</i>
TP2	<i>GP_1-5_Tompouce_02.1-6</i>	<i>Tompouce_02</i>
TP3	<i>GP_1-5_Tompouce_03.1-9</i>	<i>Tompouce_03</i>